Ore Geology Reviews 100 (2018) 263–279

Contents lists available at ScienceDirect

Ore Geology Reviews

journal homepage: www.elsevier.com/locate/oregeo

Alteration zonation and short wavelength infrared (SWIR) characteristics of the Honghai VMS Cu-Zn deposit, Eastern Tianshan, NW China

Jianhan Huang [a,b], Huayong Chen [a,c,d,*], Jinsheng Han [a], Xiaohua Deng [e], Wanjian Lu [a,b], Runliang Zhu [a,d]

[a] Key Laboratory of Mineralogy and Metallogeny, Guangzhou Institute of Geochemistry, Chinese Academy of Sciences, Guangzhou 510640, China
[b] University of Chinese Academy of Sciences, Beijing 100049, China
[c] State Key Laboratory of Ore Deposit Geochemistry, Institute of Geochemistry, Chinese Academy of Sciences, Guiyang 550002, China
[d] Guangdong Provincial Key Laboratory of Mineral Physics and Materials, Guangzhou 510640, China
[e] Beijing Institute of Geology for Mineral Resources, Beijing 100012, China

ARTICLE INFO

Article history:
Received 4 November 2016
Received in revised form 22 February 2017
Accepted 27 February 2017
Available online 24 March 2017

Keywords:
Short wavelength infrared spectra (SWIR)
White mica
Chlorite
Honghai VMS Cu-Zn deposit
Eastern Tianshan (NW China)

ABSTRACT

The Honghai VMS Cu-Zn deposit is located in the Dananhu-Tousuquan arc, Eastern Tianshan, northwestern China. Orebodies of the Honghai deposit are buried 300 m underground and hosted by the Middle Ordovician-Upper Silurian Daliugou Formation felsic to intermediate volcanic-sedimentary rocks. At the footwall and hanging wall of the massive sulfide lens, intensive and pervasive phyllic alterations were found. Detailed drill core logging, petrographic study and electron microprobe analyses had delineated six alteration/mineralization zones, namely (from top to bottom) Zone I (chlorite-albite-white mica-carbonate), II (epidote-chlorite-albite-white mica-carbonate), III (quartz-white mica-pyrite), IV (massive sulfide), V (chlorite-pyrite ± white mica) and VI (chlorite-quartz-white mica).

Our new data supported the sub-seafloor replacement influence for the Honghai VMS deposit, as evidenced by the presence of (1) sulfide breccias in the immediate host rocks; (2) rapid emplacement of host rocks; (3) strong phyllic alteration in the immediate hanging wall; (4) replacement textures of the massive sulfides; (5) barite as gangue minerals. Moreover, intensive chlorite and epidote alterations and vein mineralization are present in the hanging wall, which are comparable with porphyry-related propylitic alteration. Besides, different mineralogy and mineral chemistry are present between chlorites from the hanging wall and footwall at Honghai, which probably suggested porphyry-style alteration and mineralization overprinting at Honghai.

Short wavelength infrared (SWIR) spectral analysis had identified mainly white mica, chlorite and epidote, and minor montmorillonite, calcite, gypsum, kaolinite and prehnite. The wavelengths of the AlOH absorption feature for white mica range from 2194 to 2221 nm, suggesting compositions from paragonite, through muscovite to phengite. The wavelengths of FeOH absorption feature for chlorite range from 2249 to 2261 nm, indicating compositions from Mg-rich to Fe-rich chlorite. According to SWIR measurements and electron microprobe analyses (EMPA), areas proximal to the massive sulfides are characterized by short wavelength of the AlOH absorption feature and high Al^{vi} content of white mica. Petrography and EMPA showed that chlorite in the ore proximal zones are more Mg-rich than that in ore distal zones. These findings indicated high temperature for the white mica formation and more seawater influx during the chlorite formation in areas near the massive sulfides. This study suggested that SWIR analysis, supported by petrographic study and EMPA, can serve as an effective tool in alteration mapping, and mineral geochemical variations are potential deposit-scale exploration vectoring tools.

1. Introduction

Short wavelength infrared (SWIR) spectral analyses have been widely used in mineral exploration since the development of field portable SWIR spectrometers in the early 1990s (Thompson et al., 1999; Chang and Yang, 2012). Successful applications of SWIR have

* Corresponding author at: Key Laboratory of Mineralogy and Metallogeny, Guangzhou Institute of Geochemistry, Chinese Academy of Sciences, Guangzhou 510640, China.
E-mail address: huayongchen@gig.ac.cn (H. Chen).

http://dx.doi.org/10.1016/j.oregeorev.2017.02.037
0169-1368/

been reported for various deposit types, including porphyry, epithermal, iron oxide-Cu-Au (IOCG) and volcanogenic massive sulfide (VMS) deposits (Thompson et al., 1999; Herrmann et al., 2001; Jones et al., 2005; Harraden et al., 2013; Tappert et al., 2013; Laakso et al., 2016).

SWIR analysis is based on reflectance and absorption in the wavelength range of 1300–2500 nm. In this spectral range, H_2O, OH, CO_3, NH_4, AlOH, FeOH and MgOH molecular bonds produce characteristic absorption features (Thompson et al., 1999). The positions of the absorption features in the spectrum are a function of the molecular bonds of the mineral (Thompson et al., 1999), which are sensitive with the subtle variations in mineral compositions (Thompson et al., 1999; Jones et al., 2005). Therefore, SWIR analysis is useful for identifying mineral groups including phyllosilicates, carbonates, sulfates, OH-bearing and NH_4-bearing minerals. SWIR analysis is also useful for determining the compositional variations of minerals such as white mica, chlorite and alunite (Jones et al., 2005; Chang et al., 2011; Laakso et al., 2015). Advantages of SWIR analysis include rapid data collection, minimal sample preparation, relatively low costs, nondestructive and effective on fine-grained hydrous minerals (Thompson et al., 1999; Chang and Yang, 2012; Harraden et al., 2013).

VMS deposits are important sources of Cu, Zn, Pb, Au and Ag in the world (Franklin et al., 2005; Galley et al., 2007). These deposits are largely formed by hot, metal-rich, reduced and acidic hydrothermal fluid mixed with cold and oxidized seawater, which leads to metals precipitation on or near the seafloor, as well as intense hydrothermal alteration along the fluid pathways (Large, 1992; Gemmell and Herrmann, 2001; Laakso et al., 2016). VMS-style alteration mineral assemblages vary with deposits, but commonly include white mica, chlorite and carbonates (Franklin et al., 1981; Jones et al., 2005). Herein, white mica refers to potassic muscovite-like minerals with compositional variation between paragonite, muscovite and phengite (van Ruitenbeek et al., 2005, 2012; Laakso et al., 2016). Illite, which has vacant interlayer cation sites, is also included in this group (Yang et al., 2011). Previous applications of SWIR on VMS deposits have shown useful in exploration vectoring to mineralization. For white mica, the AlOH absorption feature shows lower wavelength in areas proximal to the orebodies, e.g., Rosebery, Western Tharsis and Highway-Reward in Australia (Herrmann et al., 2001) and Myra Falls and Izok Lake in Canada (Jones et al., 2005; Laakso et al., 2016). However, the opposite is true for some other VMS deposits, such as Hellyer in Australia and Arroyo Rojo in Argentina (Yang et al., 2011; Biel et al., 2012).

The Honghai VMS Cu-Zn deposit (discovered in 2008) is located in the Kalatag area, Eastern Tianshan (NW China), with a metal reserve of 0.27 Mt Cu (@ 1.49%), 0.27 Mt Zn (@ 3.51%), 7.1 t Au (@ 0.6 g/t) and 281 t Ag (@ 26 g/t) (Mao et al., 2010; Deng et al., 2016). Previous research of the Honghai Cu-Zn deposit has focused on its ore geology, age and isotopic geochemistry (Mao et al., 2010; Mao, 2014; Mao et al., 2015, 2016; Deng et al., 2016,2018), yet detailed studies on alteration mineralogy, alteration zonation, mineral paragenesis, SWIR and mineral chemistry are still absent. In this paper, we have (1) studied the alteration zonation and paragenesis of the Honghai deposit based on detailed core logging, thin section petrographic observation and EMPA; (2) Applied SWIR spectral analyses to determine the alteration mineralogy and features; (3) Integrated SWIR and EMPA to determine the compositional variations of white mica and chlorite, and to find any vectoring trends to the mineralization, and finally; (4) Discussed the fluid flow pathways and implications on the Honghai metallogeny.

2. Geologic setting

The Central Asia Orogenic Belt (CAOB) is one of the largest accretionary orogens on the planet, which is a consequence of Paleozoic orogenic activity mainly including a series of subduction-related accretions to the southern margin of Eurasia (Jahn et al., 2000; Xiao et al., 2013; Zheng et al., 2015; Deng et al., 2016). The Eastern Tianshan terrane is located in the southern margin of CAOB, bounded to the north and south by the Tuha and Tarim basins, respectively (Fig. 1a, Zheng et al., 2015). The Eastern Tianshan can be subdivided into, from north to south, the Dananhu-Tousuquan Arc, Kanggur Shear Zone, Yamansu Arc and the Central Tianshan Massif, separated by E-trending faults, i.e., the Kanggur, Yamansu and Aqikekuduke faults, respectively (Fig. 1b-c). The Dananhu-Tousuquan Arc comprises Ordovician-Carboniferous volcanic-sedimentary rocks, the Kanggur Shear Zone and Yamansu Arc are made up of Carboniferous-Permian volcanic-sedimentary rocks, whereas the Central Tianshan Massif comprises Precambrian metamorphic rocks. The Ordovician-Silurian calc-alkaline volcanic rocks occur along the southern margin of the Tuha Basin, whereas the Devonian rocks are consisted of mafic and pyroclastic rocks, clastic sediments and calc-alkaline felsic volcanic lavas and tuffs, and the Carboniferous rocks include lavas, pyroclastic rocks, greywacke and carbonates. The Ordovician-Silurian rocks are interpreted to be formed in active margin, while the Devonian-Carboniferous basalt and andesite display an island arc geochemical affinity (Xiao et al., 2013 and references therein). Ore deposits in the Dananhu-Tousuquan belt include the large Tuwu-Yandong porphyry Cu deposits, Xiaorequanzi VMS Cu-Zn deposit and the Kalatag Cu polymetallic belt (Mao et al., 2010; Shen et al., 2014; Deng et al., 2018).

The Kalatag district (91°40′ to 92°00′ E, 40°35′ to 42°43′ N), situating in the northern part of the Dananhu-Tousuquan arc, is composed of Paleozoic volcanic-sedimentary rocks (Fig. 2; Deng et al., 2016). Situated on the core of an anticline, the Kalatag region contains the Middle Ordovician-Upper Silurian Daliugou Formation, Silurian Hongliuxia Formation, Devonian Dananhu Formation, Carboniferous Qishan Formation and the Permian Arbasay Formation (Fig. 2). The Daliugou Formation contains three units: (from bottom to top) Unit 1 contains Na-rich basalt and basaltic andesite, Unit 2 is dominated by tuff, tuffaceous breccia and pyroclastic dacite, and Unit 3 is mainly composed of dacitic lava and breccia (Deng et al., 2016,2018). Ore deposits in the Kalatag district are mainly hosted in the Daliugou and the Hongliuxia formations (Fig. 2)

Intrusive rocks at Kalatag comprise mainly the Silurian Kalatag pluton and Devonian-Carboniferous porphyries (Fig. 2). The Kalatag pluton is situated in the southeastern Kalatag area (Fig. 2), with an exposed area of 74 km^2 (Li et al., 2006) and contains tonalite, granodiorite and monzogranite (zircon U-Pb ages: ca. 429–426 Ma, Mao, 2014). The Devonian-Carboniferous porphyries include granodiorite, monzogranite, quartz porphyry and gabbro (Mao et al., 2015), among which the granodiorite in the Yudai and Xierqu mining districts yielded zircon U-Pb ages of ca. 387–382 Ma and quartz porphyry in the Meiling mining district yielded zircon U-Pb age of ca. 300 Ma (Mao, 2014).

The NNW-trending Kalatag fault and the E-trending Kabei fault represent the southern and northern boundaries of the Kalatag district, respectively. The Kabei fault extends for 35 km, dipping north at 60–65°. The Kalatag fault is 50 km long and up to 0.5 km wide, dipping north at 60° and controls the distribution of the Early Paleozoic magmatism (Mao et al., 2015; Deng et al., 2018). NW-, NNW- and N-trending faults control the volcanism and mineralization at Kalatag (Deng et al., 2016,2018).

Six deposits are present at Kalatag, including the Yudai porphyry Cu, Xierqu skarn Fe-Cu, Hongshan epithermal Cu-Au, Hong-

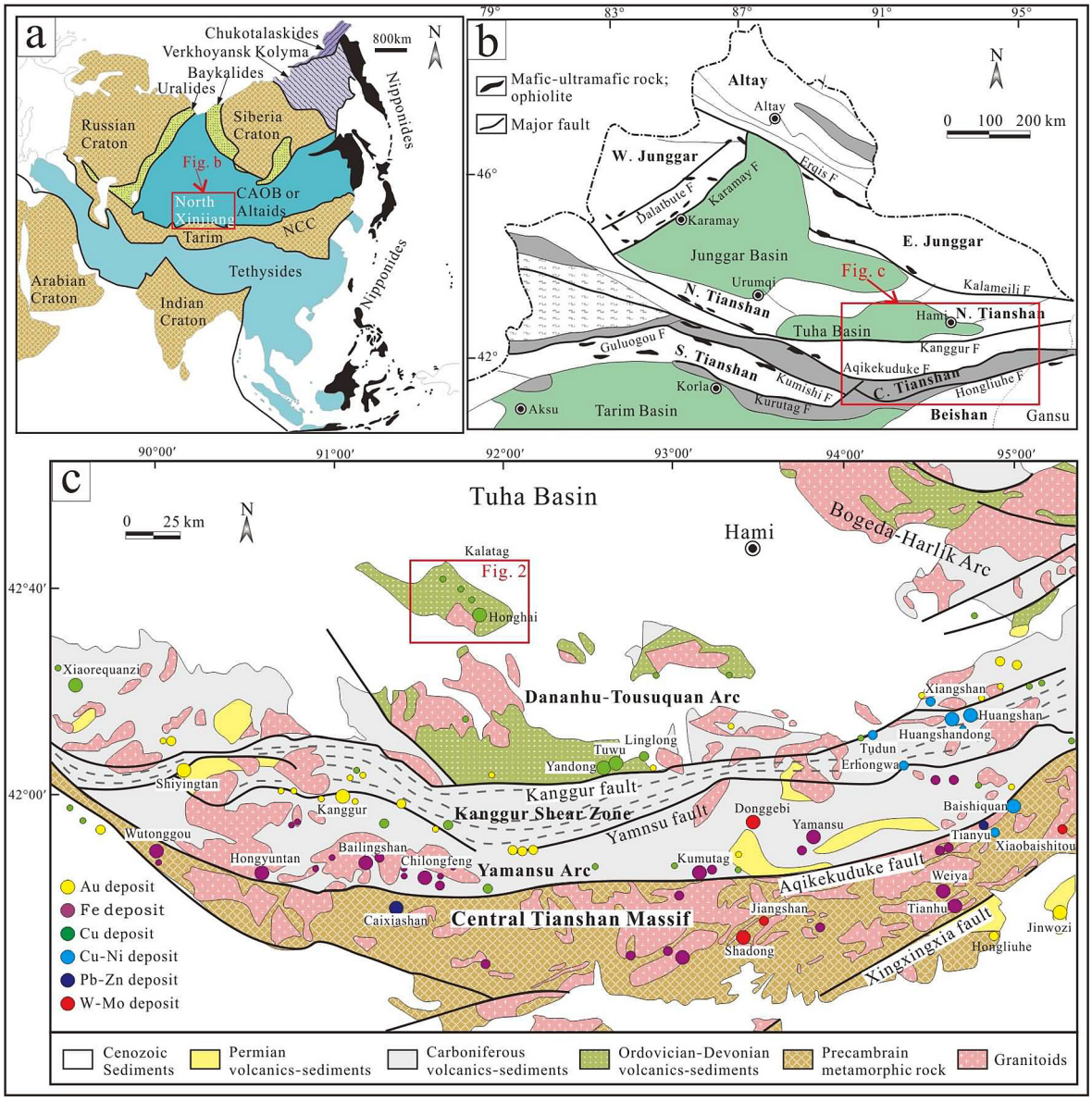

Fig. 1. a. Schematic map showing the location of northern Xinjiang (modified after Sengör et al., 1993). b. Sketch map showing the major tectonic units in northern Xinjiang (modified after Chen et al., 2012). c. Tectonic framework and distribution of major ore deposits in Eastern Tianshan (modified after Wang et al., 2006).

shi and Meiling hydrothermal vein Cu, and the Honghai VMS Cu-Zn deposits (Fig. 2; Mao et al., 2010, 2015; Deng et al., 2014). Latest exploration has delineated metal reserves of about 0.69 Mt Cu, 0.29 Mt Zn and 7.79 t Au in the Kalatag district (Deng et al., 2016).

3. Deposit geology

The Honghai VMS Cu-Zn deposit is located in the southeastern part of the Kalatag district. The Honghai stratabound or lensoid orebodies are hosted along the Unit 2 – Unit 3 contact of the Daliugou Formation felsic to intermediate volcanic-sedimentary rocks (Fig. 3). The footwall alteration mainly consists of phyllic and chlorite alterations with stockworks or disseminated Cu mineralization, while the hanging wall alteration is dominated by chlorite, epidote, albite and silicic alterations.

The Honghai Cu-Zn deposit contains metal reserves of 0.27 Mt Cu @ 1.49%, 0.27 Mt Zn @ 3.51%, 7.1 t Au @ 0.6 g/t and 281 t Ag @ 26 g/t (Deng et al., 2016a). Individual orebody is 1100 m long, 53 m wide, and dipping NE at 40–75° (Deng et al., 2016). The massive sulfide orebody, hosting >60 vol.% of the Honghai sulfides, is the main metal reserve. Besides, banded, brecciated and disseminated ores are also present outside the massive sulfide orebody (Mao et al., 2015, 2016). Veins and disseminated ores are developed in the immediate footwall of the main ore lens, which probably represent the feeder zone of a sub-seafloor hydrothermal system (Deng et al., 2016).

Ore textures include subhedral-anhedral granular, skeleton, relict and exsolution textures (Mao et al., 2015, 2016). Pyrite, chalcopyrite and sphalerite are the dominant metallic minerals, with minor Ag-bearing tennantite, galena and pyrrhotite. Gangue minerals include mainly quartz, chlorite, white mica, barite and carbonates.

4. Samples and methods

4.1. Sampling

In this study, a total of 520 rock samples were collected from 21 drill holes within and immediately around the Honghai VMS

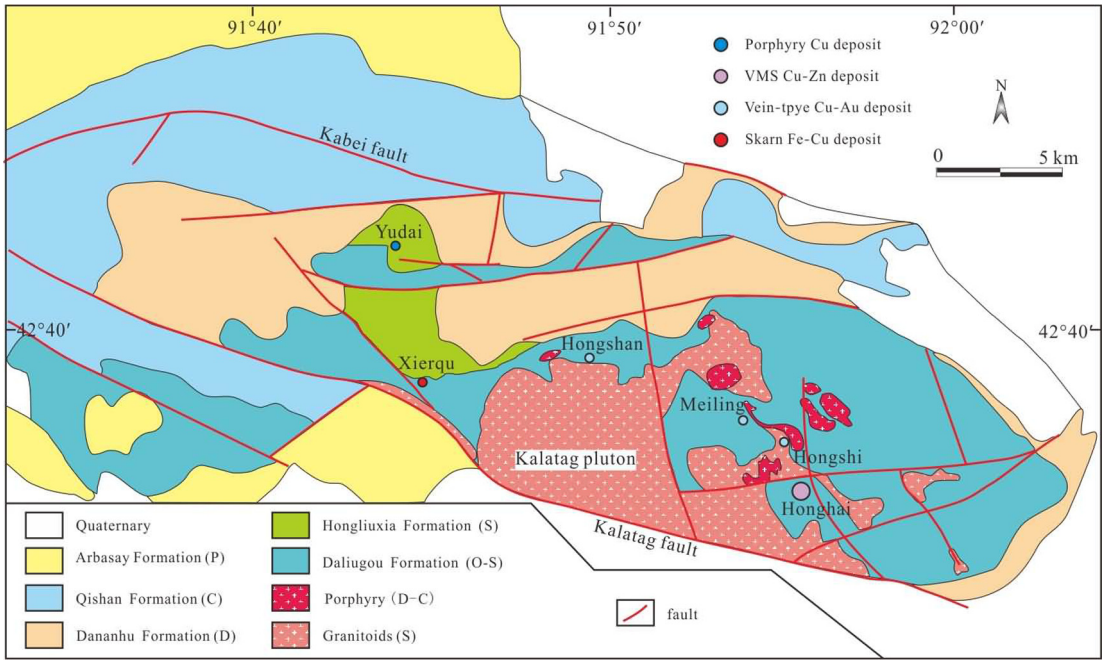

Fig. 2. Geologic map of the Kalatag district (modified after Deng et al. (2016,2018)).

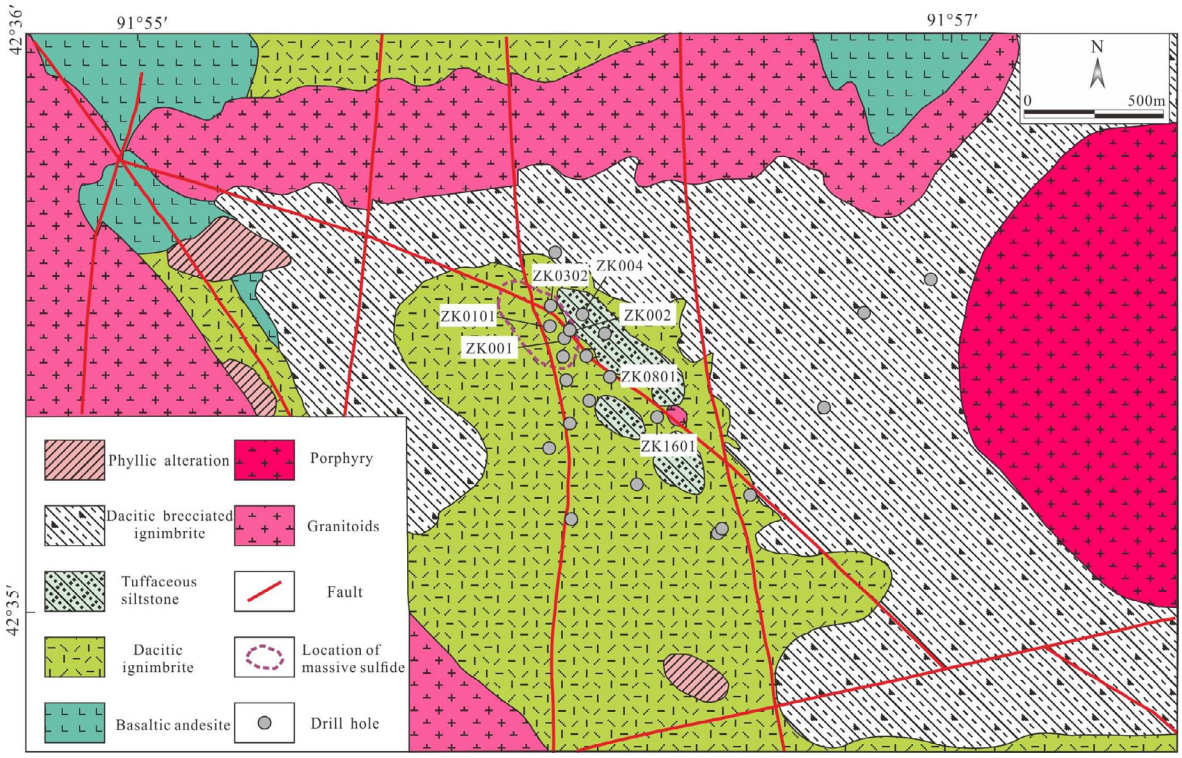

Fig. 3. Geologic map of the Honghai Cu-Zn deposit (modified after Mao et al., 2015).

deposit. The sampling interval was about 20 m, and decreased where the alteration and mineralization intensify or lithology changes. 43 samples (mostly mineralized) were collected in underground mining tunnels. About 250 polished thin sections were prepared for representative samples, and were studied under the microscope.

4.2. SWIR spectral analysis

Sample preparation for SWIR spectral analysis was minimal, with spectral collected on clean, dry drill core samples. 1528 near-infrared and SWIR spectra were obtained on 510 drill core samples (10 samples were excluded due to the presence of large

amounts of sulfides) with a TerraSpec made by Analytical Spectral Devices, Inc (ASD). Three analyses were commonly measured on one sample within three circled spots. RS^3 software was used to collect the SWIR spectra, settings in the TerraSpec signal collection were as outlined in Chang and Yang (2012).

Mineral identification and mineral abundance estimation were based on the intensity, wavelength and shape of the main absorption features in each spectrum, and on comparing the spectra with a reference library using The Spectral Geologist (TSG) software. The numerical parameters, including wavelength position and absorption depth of white mica AlOH and chlorite FeOH absorption features, were extracted using the Scalar function of TSG, and settings for the acquisition parameters were as outlined in Chang and Yang (2012) and Yang et al. (2012).

In SWIR band, H_2O, OH, CO_3, NH_4, AlOH, FeOH and MgOH molecular bonds produce characteristic absorption features. The combination of these absorption features make it possible to determine mineral groups including phyllosilicates, carbonates, sulfates, OH-bearing and NH_4-bearing minerals (Thompson et al., 1999; Jones et al., 2005).

4.3. EMPA

EMPA was conducted on a JEOL JXA-8230 electron probe microanalyser at the Key Laboratory of Mineralogy and Metallogeny, Guangzhou Institute of Geochemistry, Chinese Academy of Sciences. Operating conditions include 15-kV accelerating voltage, 20 nA probe current and 1-μm beam diameter. The minerals analyzed include chlorite, epidote, white mica, pyrite, chalcopyrite, sphalerite and tennantite. Mineral formulas were calculated on the basis of 22 oxygens for white mica and 28 oxygens for chlorite.

5. Alteration/mineralization zonation and paragenesis

5.1. Alteration types and zonation

Pervasive alteration is developed below the Honghai massive sulfide orebody and in the volcanic-sedimentary hanging wall rocks. Major alteration types include phyllic, chlorite, epidote, albite, silicic and carbonate alterations (Fig. 4). Phyllic alteration (quartz + white mica + pyrite) is associated with the massive sulfide mineralization, and is mainly distributed in the footwall and immediate hanging wall. Chlorite alteration is distributed in both the footwall and the volcanic-volcaniclastic hanging wall rocks. Epidote and albite alterations are mainly present in the hanging wall, whereas carbonate alteration commonly occurs as veins or patches in both the footwall and the hanging wall of the Honghai deposit.

Detailed drill core logging and petrographic study have delineated six alteration/mineralization zones, which comprise (top to bottom) the chlorite-albite-white mica-carbonate, epidote-chlorite-albite-white mica-carbonate, quartz-white mica-pyrite, massive sulfide, chlorite-pyrite ± white mica and chlorite-quartz-white mica zones (Fig. 4; Table 1).

5.1.1. Chlorite-albite-white mica-carbonate zone

It extends from the ground surface to about 150 m deep, and is dominated by chlorite, albite and white mica, with minor carbonate and trace pyrite and epidote. Gypsum and hematite are present in fractures.

5.1.2. Epidote-chlorite-albite-white mica-carbonate zone

It extends below the chlorite-albite-white mica-carbonate zone for over 200 m. Epidote, chlorite, albite and quartz dominate this

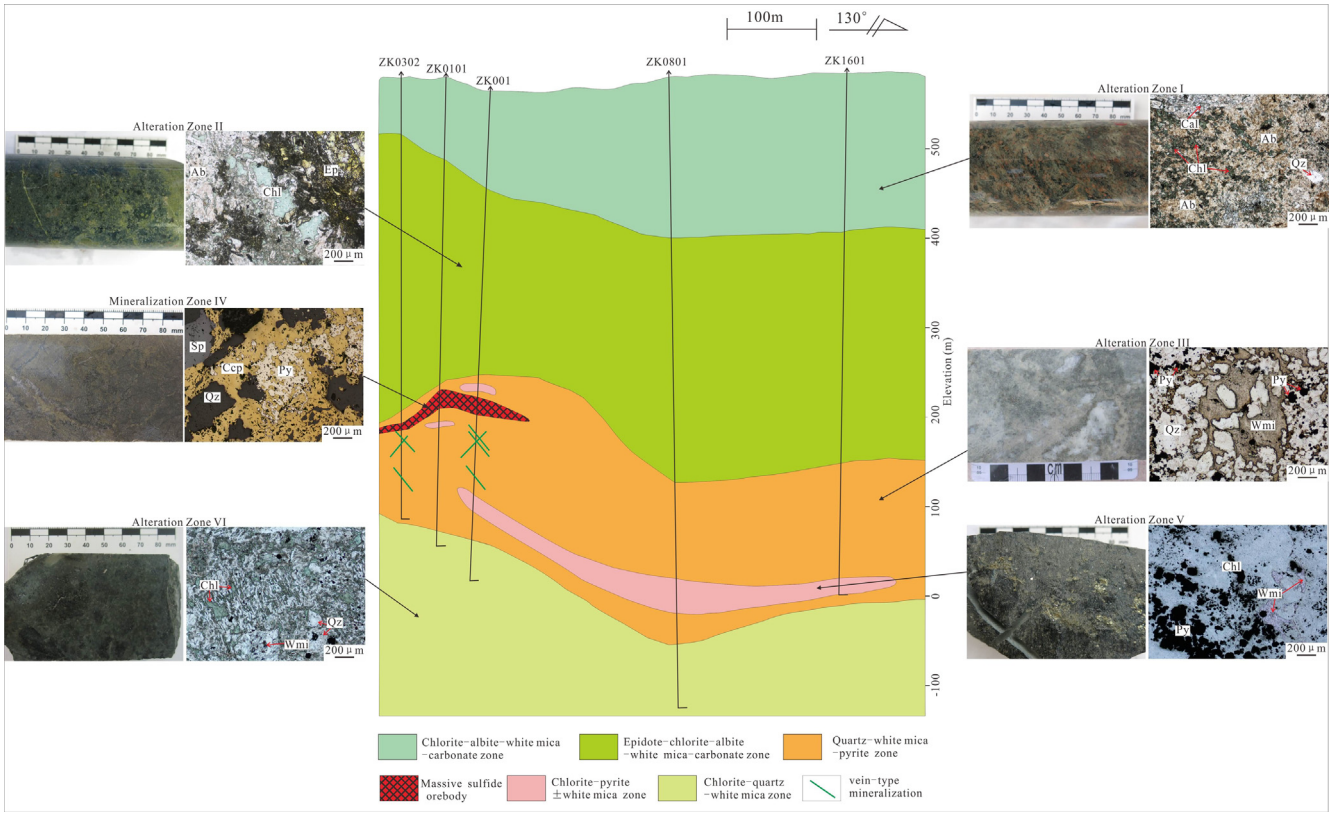

Fig. 4. Alteration zonation and characteristic photographs and photomicrographs in a cross section of the Honghai Cu-Zn deposit. Abbreviations: Ab = albite, Cal = calcite, Chl = chlorite, Qz = quartz, Ep = epidote, Py = pyrite, Wmi = white mica, Ccp = chalcopyrite, Sp = sphalerite.

Table 1
Mineral assemblages of the alteration/mineralization zones at Honghai.

No.	Alteration zone	Major minerals	Minor-trace minerals
I	Chlorite-albite-white mica-carbonate zone	Chlorite, albite, quartz	Calcite, white mica, hematite, epidote, pyrite, gypsum
II	Epidote-chlorite-albite-white mica-carbonate zone	Epidote, chlorite, albite, quartz	Calcite, white mica, hematite, specularite, magnetite, chalcopyrite, bornite, digenite, covellite
III	Quartz-white mica-pyrite zone	Quartz, white mica, pyrite	Chalcopyrite, sphalerite, calcite, chlorite
IV	Massive sulfide zone	Pyrite, sphalerite, chalcopyrite	Barite, quartz, tennatite, galena, white mica-muscovite, magnetite
V	Chlorite-pyrite ± white mica zone	Chlorite, pyrite	White mica, chalcopyrite, quartz
VI	Chlorite-quartz-white mica	Quartz, chlorite, white mica	Pyrite, calcite, chalcopyrite, bornite

zone (Fig. 4), with small amounts of white mica, calcite, Fe-oxides and Cu sulfides. The Cu sulfides are associated with epidote, and include chalcopyrite, bornite, digenite and covellite.

5.1.3. Quartz-white mica-pyrite zone

It is most common in the footwall and extends up to 20 m to the immediate hanging wall of the massive sulfide lens. Quartz, white mica and pyrite are the major minerals (Fig. 4), with minor chalcopyrite, sphalerite, chlorite and calcite. Despite the intensive alteration, primary volcanic textures (e.g., laminated and brecciated) are still preserved. Quartz + pyrite ± chalcopyrite and pyrite + chalcopyrite veins are present below the massive sulfide lens of the phyllic alteration zone, whereas late quartz + carbonate veins crosscut the phyllic alteration.

5.1.4. Massive sulfide zone

It is mainly hosted in the quartz-white mica-pyrite zone, and extends up to 40 m thick. Sulfide minerals account for >60 vol.% of the massive sulfide orebody, and include mainly pyrite, chalcopyrite and sphalerite, and minor tennantite, galena and pyrrhotite (Fig. 4). Copper-bearing veins are present in the immediate footwall of the massive sulfide orebody, which are interpreted to be the feeder zone or stockworks of a sub-seafloor hydrothermal system (Deng et al., 2016).

5.1.5. Chlorite-pyrite ± white mica zone

It is commonly developed in the footwall of the massive sulfide lens, yet it is also locally present in the immediate hanging wall. The zone is characterized by chlorite and pyrite, with minor white mica, quartz and chalcopyrite.

5.1.6. Chlorite-quartz-white mica zone

It is intersected at the bottom of the drill holes. Mafic-intermediate minerals in the basalt and basaltic andesite are replaced by chlorite, quartz and white mica, and minor epidote grains and carbonate veins are also present. Minor disseminated chalcopyrite and bornite mineralization is present, which is associated with chlorite.

5.2. Mineralization paragenesis

Based on mineral assemblages and their replacement/crosscutting relationships, three mineralization periods (seven stages) are recognized, i.e., the VMS, hydrothermal overprinting and supergene mineralization periods. The VMS period can be subdivided into the pyrite, chalcopyrite-sphalerite and barite stages, whilst the hydrothermal overprinting period can be subdivided into the albite, chlorite-epidote and quartz-carbonate stages (Fig. 5).

5.2.1. VMS period

Pyrite stage is dominated by pyrite, quartz and white mica (Fig. 6a). Pyrite occurs as aggregates or subhedral-euhedral indi-

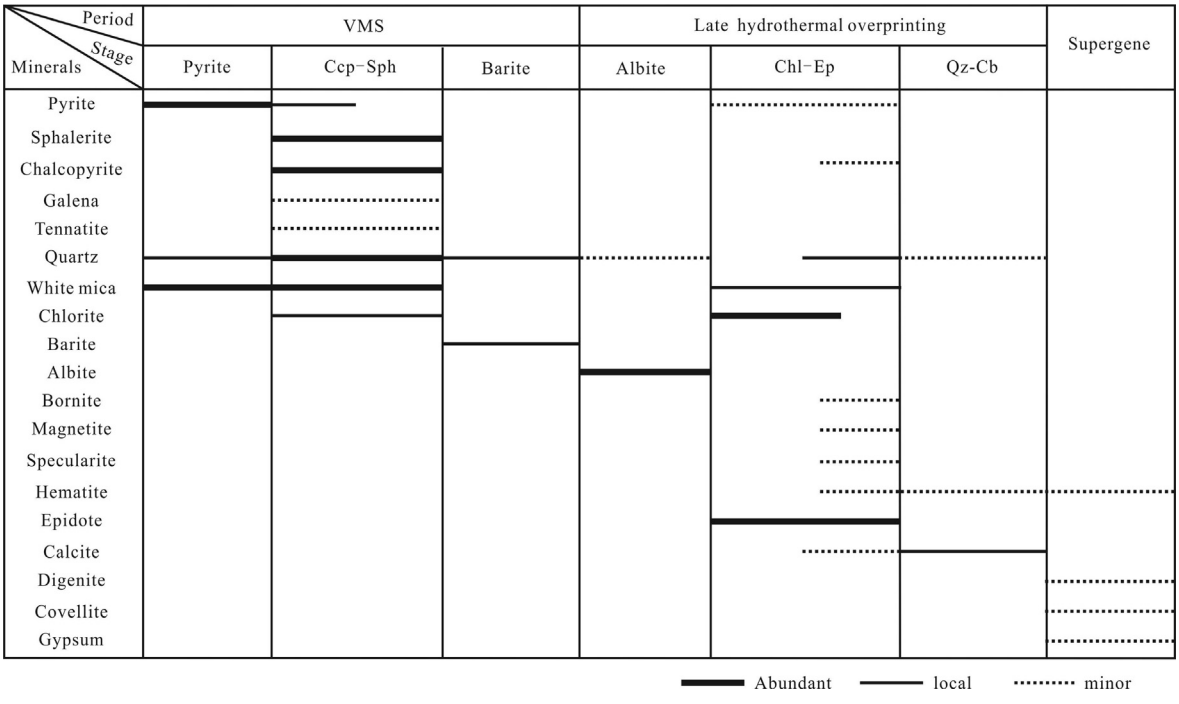

Fig. 5. Paragenetic sequence of the Honghai Cu-Zn deposit.

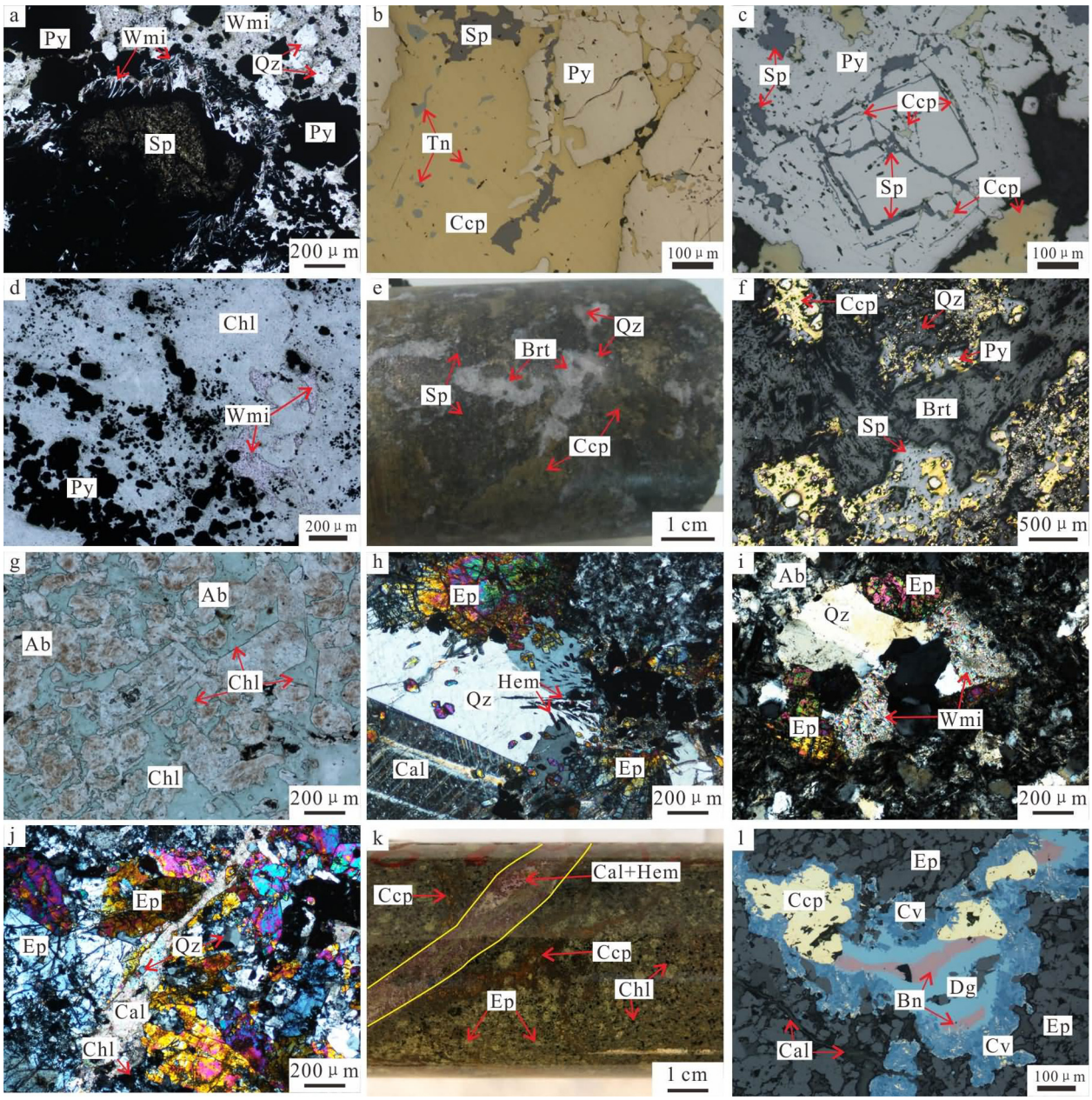

Fig. 6. Characteristic photographs and photomicrographs showing the mineralization periods of the Honghai deposit. a. Phyllic alteration (quartz + white mica + pyrite) and sphalerite; b. Chalcopyrite-sphalerite-tennatite replaced pyrite; c. Sphalerite-chalcopyrite filled along fractures of pyrite; d. Chlorite alteration and minor white mica; e. Barite and quartz crosscut the massive sulfide ore; f. Barite vein crosscut pyrite, chalcopyrite and sphalerite; g. Albite alteration was replaced by chlorite; h. Typical quartz + calcite + epidote ± hematite vein; i. Patch of epidote + white mica + quartz; j. Calcite + quartz vein crosscut epidote and chlorite alteration; k. Calcite + hematite vein crosscut chalcopyrite and epidote, chlorite; l. Chalcopyrite and bornite replaced by digenite and covelite. Abbreviations: Py = pyrite, Qz = quartz, Sp = sphalerite, Wmi = white mica, Ccp = chalcopyrite, Tn = tennatite, Chl = chlorite, Brt = barite, Ab = albite, Ep = epidote, Cal = calcite, Hem = hematite, Bn = bornite, Cv = covellite, Dg = digenite.

vidual grains, with euhedral muscovite occurred inside pyrite or along its margin. The *chalcopyrite-sphalerite stage* contributes the majority of the Honghai metal resources. At this stage, chalcopyrite and sphalerite commonly replaced pyrite or filled in the fractures or space among pyrite grains (Fig. 6b-c). Chalcopyrite often has straight boundaries with sphalerite, or occurs as exsolution in sphalerite. Pyrite is also present in this stage, which is associated with chlorite (Fig. 6d). Minor to trace amount of tennantite and galena present highly associated with sphalerite or chalcopyrite (Fig. 6b), which indicate that tennantite and galena were formed at the same stage with sphalerite and chalcopyrite. Barite and quartz at *barite stage* occur as veins that crosscut minerals of the pyrite and chalcopyrite-sphalerite stages (Fig. 6e-f).

5.2.2. Hydrothermal overprinting period

This period was found in the over 300 m thick volcanic-sedimentary hanging wall rocks, suggesting that the period was post-VMS mineralization. *Albite stage* is characterized by intense albite alteration with minor quartz. Albite alteration appears as pink disseminations or patches in hand specimen, and is replaced or crosscut by chlorite and epidote. Under the microscope, the secondary albite occurs mainly as granular aggregates and minor as euhedral columnar crystals (Fig. 6g). *Chlorite-epidote stage* is dominated by intense chlorite-epidote alteration, with moderate to minor white mica, quartz and calcite (Fig. 6h-j). Chlorite (disseminated, banded or spotty) replaced mafic minerals, feldspar and groundmass, and contains plenty of small quartz inclusions

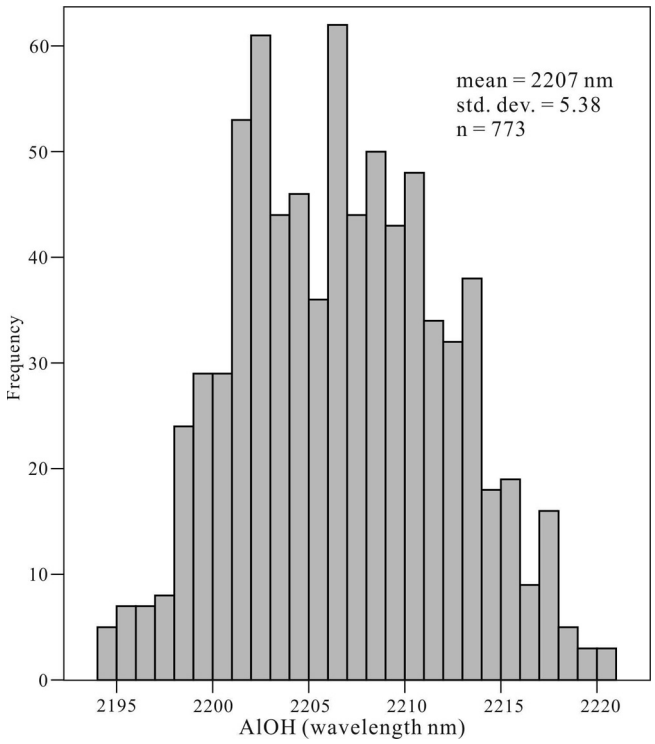

Fig. 7. Histogram of the wavelength range of the AlOH absorption feature for the Honghai white mica.

(several μm). Epidote + quartz + calcite ± hematite veins and disseminated epidote are common (Fig. 6h). Minor chalcopyrite and bornite mineralization was also developed, and was generally associated with epidote. *Quartz-carbonate stage* is dominated by quartz + carbonate ± hematite veins, which crosscut rocks/ores of the VMS period, and the albite stage and chlorite-epidote stages (Fig. 6j-k). Carbonate is dominated by calcite, with minor ankerite.

5.2.3. Supergene period

Minor amounts of digenite, covellite and hematite at this period are mainly weathering products of chalcopyrite, bornite and pyrite of the VMS and hydrothermal overprinting periods (Fig. 6l). Gypsum is present mainly in fractures.

5.3. Mineral compositions

5.3.1. Chlorite

Chlorite of the VMS period is mainly distributed in the footwall and immediate hanging wall of the Honghai massive sulfide lens (alteration zones III, V and VI). The VMS-mineralization-related chlorite (Chlorite I) is associated with pyrite, and minor white mica, quartz and chalcopyrite. It is deep green in hand specimen, light to medium green under plane-polarized light and gray or grayish-green under cross-polarized light (defined as Mg-rich chlorite by Kranidiotis and MacLean (1987)). Chlorite of the hydrothermal overprinting period (Chlorite II) is distributed in the volcanic-sedimentary hanging wall rocks, and is associated with epidote, albite, white mica and calcite. This chlorite is medium to deep green in plane-polarized light, anomalous blue and violet under cross-polarized light (defined as Fe-rich chlorite by Kranidiotis and MacLean (1987)).

At Honghai, Chlorite I and II are chemically distinguishable. Chlorite I contains 17.43–24.14 (avg. 20.36) wt.% FeO and 15.94–21.60 (avg. 18.46) wt.% MgO, whereas Chlorite II has 21.23–33.66 (avg. 26.23) wt.% FeO and 9.32–19.46 (avg. 15.07) wt.% MgO. All chlorites have narrow ranges of SiO_2 (24.53–28.07 wt.%) and Al_2O_3 (18.30–21.61 wt.%). Chlorite I is more Mg-rich and Fe-poor than Chlorite II, and there is a general Mg increase from the alteration/mineralization zone I to V. According to the Hey's classification diagram (Hey, 1954), all chlorites plot in the ripidolite and pycnochlorite fields, with 5.32–5.71 Si atoms per formula unit and Fe/(Fe + Mg) ratios of 0.31 to 0.67.

5.3.2. Sulfides

EMPA of pyrite in the Honghai massive sulfide lens (pyrite stage) show low concentrations of Cu, Zn, As, Pb and Co. Concentrations of Te, Cd, Ni and Ag are even below the detection limit, Gold content can be up to 0.05 wt.%.

Chalcopyrite contains 0.02–0.04 wt.% Au, and low concentrations of Zn, Pb, Co and Ag. Sphalerite contains 0.74–1.11 wt.% Fe and 0.20–0.26 wt.% Cd, up to 0.02 wt.% Au, with trace Cu, Te, Co and Ni.

Tennantite shows high Ag contents (0.57–5.6 wt.%), indicating that tennantite is the main Ag-bearing mineral at Honghai. Besides As and Cu, Fe (3.42–9.19 wt.%) and Zn (4.14–5.42 wt.%) are also high in tennantite. They also have low contents of Cd and Co, with occasionally trace Ni, Co, Pb and Au.

6. SWIR spectral analysis

6.1. Alteration minerals

The SWIR analysis results show that the AlOH absorption feature is mainly associated with white micas and the FeOH absorption feature is associated with chlorite and epidote. However, the spectral data and the petrographic results are not perfectly consistent. Firstly, different sizes and areas between thin sections (<26 × 46 mm) and SWIR spectral measurements (100 mm^2) yielded an incomplete correlation. Secondly, because the absorption coefficients of carbonates are significantly weaker than chlorite and epidote (Herrmann et al., 2001), carbonates (dominantly calcite) in most samples were not identified by spectral analyses. Thirdly, epidote has similar FeOH and MgOH absorption features with chlorite, and thus these two minerals would be easily mixed

Table 2
Summary statistics of white mica AlOH and chlorite FeOH absorption features of the Honghai deposit.

		Minimum (nm)	Maximum (nm)	Mean (nm)	Median (nm)	Range (nm)	N
AlOH	Zone I	2202	2219	2209	2209	17	124
	Zone II	2199	2221	2211	2211	22	291
	Zone III	2194	2210	2202	2202	16	230
	Zone V & VI	2198	2214	2205	2204	16	60
FeOH	Zone I	2250	2259	2255	2255	9	112
	Zone II	2249	2258	2254	2254	9	362
	Zone III	2250	2257	2252	2252	7	36
	Zone V & VI	2251	2261	2253	2253	10	81

up when other absorption features in epidote are not distinct (in low proportion).

Of the 1528 SWIR spectra obtained from the Honghai drill core samples, 41 spectra were discarded due to low signal-to-noise ratios. White mica, chlorite, epidote, montmorillonite, calcite, gypsum, kaolinite and prehnite were identified, among which 575 spectra indicate only one mineral, including white mica, chlorite, epidote, calcite, gypsum and prehnite, whilst the other spectra showed two or more minerals, dominated by white mica + chlorite, white mica + epidote, chlorite + epidote and white mica + chlorite + epidote. The uncommon kaolinite, montmorillonite, calcite and gypsum usually mix with white mica and/or chlorite.

White mica has a sharp, deep, single AlOH absorption feature between 2186 and 2225 nm and weaker secondary AlOH absorption features near 2344 and 2440 nm (Herrmann et al., 2001; Jones et al., 2005; Chang and Yang, 2012). SWIR analyses showed that white mica is the most common alteration mineral in most of the Honghai alteration/mineralization zones (except the massive sulfide zone). 1039 spectral measurements were indicated to contain white mica, among which 274 spectra contain only white mica, and the rest show variable degrees of mixing with one or two mineral(s), which are typically chlorite and/or epidote, and less commonly calcite, kaolinite, montmorillonite and gypsum.

Chlorite spectra have diagnostic FeOH and MgOH absorption features near 2250 nm (ranging 2235–2265 nm) and 2340 nm (ranging 2320–2360 nm), respectively (Herrmann et al., 2001; Jones et al., 2005). SWIR analyses show that chlorite alteration is the second most intensive alteration type at Honghai, and is common in most alteration zones except in the quartz-white mica-pyrite zone. Chlorite was found in 639 spectra from 372 rock samples, among which 108 spectra show chlorite-only, 376 spectra show mixing with white mica, 63 spectra show mixing with epidote, 63 spectra show mixing with white mica and epidote, and the rest show mixing with gypsum and montmorillonite.

Epidote also has FeOH and MgOH absorption features near 2250 nm and 2350 nm, respectively, but the FeOH absorption feature is distinctly weaker than that of chlorite. Epidote is abundant

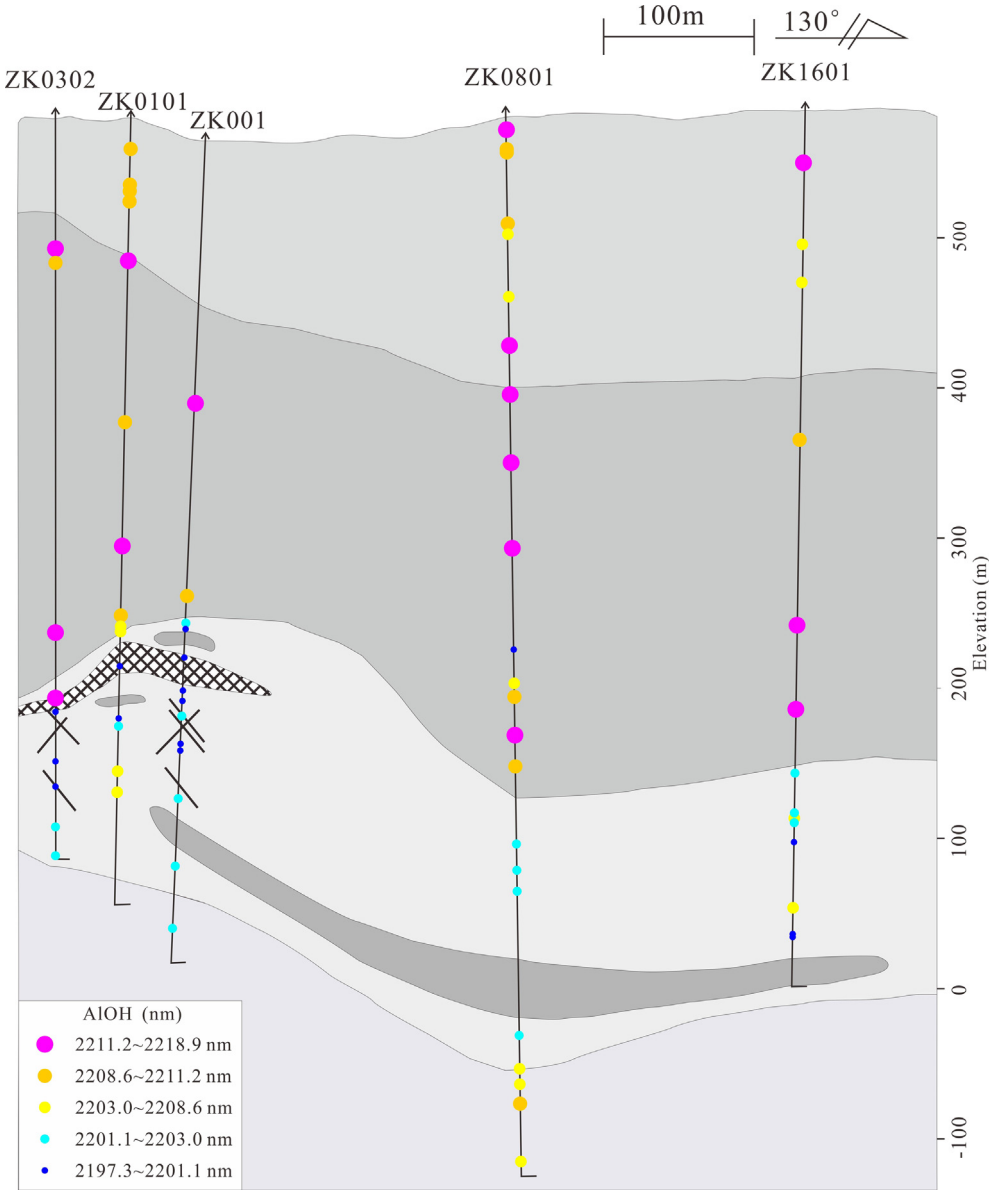

Fig. 8. Wavelength of the AlOH absorption feature of white mica from the NW section of the Honghai deposit.

Table 3
EMPA results for the Honghai white mica.

Alteration zone	I		II					III											IV	V & VI	
Sample no.	ZK0801-2 (4)	ZK0801-5 (2)	ZK001-1 (2)	ZK0302-10 (2)	ZK0302-11 (7)	ZK0302-14 (3)	ZK1601-10 (3)	ZK001-9 (8)	ZK001-11 (4)	ZK001-14 (6)	ZK001-19 (4)	ZK001-21 (5)	ZK0302-16 (4)	ZK0302-19 (4)	ZK0302-23 (5)	ZK0801-23 (5)	ZK0801-27 (4)	ZK1601-19 (5)	HH2206-4 (2)	ZK1601-25 (2)	ZK0801-32 (3)
AlOH (nm)	2209				2211	2211		2199	2201	2197	2202	2202	2199	2198	2202	2202		2203			2207
wt.%																					
SiO_2	48.04	50.15	50.29	52.33	51.39	51.58	49.99	50.77	49.34	49.21	50.43	49.55	46.09	50.07	48.75	50.01	49.39	48.67	48.06	48.71	48.62
TiO_2	0.10	0.09	0.26	0.10	0.01	0.16	0.13	0.19	0.13	0.07	0.19	0.14	0.27	0.09	0.10	0.11	0.12	0.15	0.04	0.17	0.15
Al_2O_3	28.91	31.10	29.13	30.88	31.18	30.17	28.36	32.45	33.58	35.38	33.40	34.42	31.30	33.15	33.17	33.92	31.99	32.16	35.06	31.32	31.84
FeO	3.16	2.65	3.94	1.66	1.27	1.07	3.62	1.42	0.99	0.56	1.17	1.29	1.58	0.77	0.95	0.69	1.22	1.17	0.61	1.96	1.94
MnO	0.04	0.02	0.02	0.01	0.01	0.02	0.02	0.01	0.02	0.00	0.02	0.01	0.01	0.01	0.01	0.01	0.00	0.02	0.03	0.02	0.03
MgO	1.35	0.97	0.98	1.80	1.49	1.73	2.07	0.74	0.82	0.64	1.18	1.41	1.02	0.50	0.84	1.02	0.69	1.26	0.40	1.44	1.86
CaO	0.17	0.16	0.04	0.15	0.15	0.22	0.07	0.13	0.20	0.11	0.07	0.09	0.07	0.13	0.10	0.09	0.06	0.12	0.08	0.08	0.11
Na_2O	0.23	0.14	0.09	0.20	0.33	0.20	0.14	0.21	0.28	0.28	0.21	0.23	0.37	0.26	0.28	0.25	0.29	0.20	0.60	0.23	0.26
K_2O	9.67	9.23	9.95	8.50	9.24	8.85	10.31	9.23	8.13	8.87	9.09	9.23	8.66	9.16	9.83	9.57	9.74	9.65	9.58	10.12	9.69
Total	91.71	94.51	94.68	95.65	95.08	94.00	94.74	95.16	95.48	96.79	96.61	96.70	89.38	94.14	94.04	95.71	93.49	93.44	94.54	94.03	94.53
apfu (calculated based on 22 oxygens)																					
Si	6.66	6.67	6.76	6.80	6.75	6.82	6.74	6.66	6.45	6.35	6.53	6.42	6.47	6.62	6.50	6.52	6.62	6.54	6.37	6.55	6.49
Al^{iv}	1.34	1.33	1.24	1.20	1.25	1.18	1.26	1.34	1.55	1.65	1.47	1.58	1.53	1.38	1.50	1.48	1.38	1.46	1.63	1.45	1.51
Al^{vi}	3.39	3.55	3.37	3.53	3.57	3.53	3.24	3.68	3.62	3.73	3.62	3.67	3.65	3.78	3.71	3.74	3.68	3.63	3.84	3.51	3.50
Ti	0.01	0.01	0.03	0.01	0.00	0.02	0.01	0.02	0.01	0.01	0.02	0.01	0.03	0.01	0.01	0.01	0.01	0.02	0.00	0.02	0.01
Fe	0.37	0.29	0.44	0.18	0.14	0.12	0.41	0.16	0.11	0.06	0.13	0.14	0.19	0.08	0.11	0.08	0.14	0.13	0.07	0.22	0.22
Mn	0.00	0.00	0.00	0.00	0.00	0.00	0.00	0.00	0.00	0.00	0.00	0.00	0.00	0.00	0.00	0.00	0.00	0.00	0.00	0.00	0.00
Mg	0.28	0.19	0.20	0.35	0.29	0.34	0.42	0.14	0.16	0.12	0.23	0.27	0.21	0.10	0.17	0.20	0.14	0.25	0.08	0.29	0.37
Ca	0.03	0.02	0.01	0.02	0.02	0.03	0.01	0.02	0.03	0.01	0.01	0.01	0.01	0.02	0.01	0.01	0.01	0.02	0.01	0.01	0.02
Na	0.06	0.04	0.02	0.05	0.08	0.05	0.04	0.05	0.07	0.07	0.05	0.06	0.10	0.07	0.07	0.06	0.08	0.05	0.15	0.06	0.07
K	1.71	1.57	1.71	1.41	1.55	1.49	1.77	1.54	1.36	1.46	1.50	1.52	1.55	1.54	1.67	1.59	1.66	1.65	1.62	1.74	1.65
Na/(Na + K)	0.035	0.023	0.013	0.035	0.051	0.032	0.021	0.033	0.049	0.046	0.035	0.037	0.061	0.041	0.041	0.039	0.043	0.031	0.086	0.033	0.04
Si/Al	1.41	1.37	1.46	1.44	1.40	1.45	1.50	1.33	1.25	1.18	1.28	1.22	1.25	1.28	1.25	1.25	1.31	1.28	1.16	1.32	1.30
Fe + Mg	0.65	0.49	0.64	0.53	0.43	0.46	0.82	0.30	0.27	0.18	0.35	0.41	0.40	0.18	0.27	0.27	0.27	0.38	0.15	0.51	0.59

in the epidote-chlorite-white mica zone, and also locally in other alteration zones.

Carbonates have diagnostic CO_3 absorption features of 2300 to 2350 nm, which overlap with the MgOH and secondary AlOH absorption features. Carbonates have significantly weaker absorption coefficients than those of phyllosilicates, and thus some veined or disseminated carbonates were unrecognized by the SWIR analysis (Herrmann et al., 2001). At Honghai, despite carbonates (dominantly calcite), were commonly identified in rock samples, only 23 spectra were interpreted to contain calcite.

6.2. Spectral and compositional variations

6.2.1. White mica

At Honghai, the AlOH absorption feature of white mica was found in 434 drill core samples (85.1% of the total samples). The wavelength position frequency distribution of the AlOH absorption feature was shown in Fig. 7, and the wavelength covers a range from 2194 to 2221 nm, with most values clustering in 2198–2214 nm (mean = 2207 nm, median = 2207 nm, n = 773). The wide wavelength range indicates that the rock samples contain white mica of diverse compositions, from slightly Na-muscovite (paragonite, wavelength near 2195 nm), through potassic (muscovite and illite, wavelength near 2200 nm) to phengitic muscovite (wavelength > 2216 nm) (Herrmann et al., 2001; Jones et al., 2005).

The white mica AlOH absorption features in different alteration zones were summarized in Table 2, including minimum, maximum, mean, median and range. The observed wavelengths in Alteration Zones I and II (mean = 2209 nm, 2211 nm) are distinctly longer than those in alteration zones III, V and VI (mean = 2202 nm, 2205 nm).

Fig. 8 shows the variations of the wavelength of the AlOH absorption feature of white mica within alteration zones in NW cross section. The AlOH absorption feature of white mica shows a spectral shifts of AlOH absorption feature from Alteration Zones I and II (>2205 nm) to Alteration Zones III, V and VI (<2205 nm). In Alteration Zones I and II, the wavelengths do not vary much with increasing depth of the drill cores, yet a systematic decrease was found in proximal alteration halos above the massive sulfide lens (Fig. 8). In contrast, for samples from Alteration Zones III, V and VI, the wavelengths increase slightly with increasing depth below the massive sulfide orebody (ZK0302, ZK0101 and ZK002).

EMPA data showed that the Honghai white mica is K-mica (average K_2O = 8.13–10.31 wt.%) (Table 3). The wavelengths of the AlOH absorption feature for white mica increase with increasing Si/Al ratio and Fe + Mg content and decreasing Al content (total Al, octahedral Al; Fig. 9). However, the negative correlation between the wavelength of the AlOH absorption feature and Na/(Na + K) ratio is poor (R^2 = 0.04), which is apparent shown in previous works (Duke, 1994; Herrmann et al., 2001; Jones et al., 2005).

Samples at the proximal zone to ore horizon (Alteration Zone III) have shorter wavelengths of the AlOH absorption feature of white mica, with average Fe + Mg content of 0.30 atoms per for-

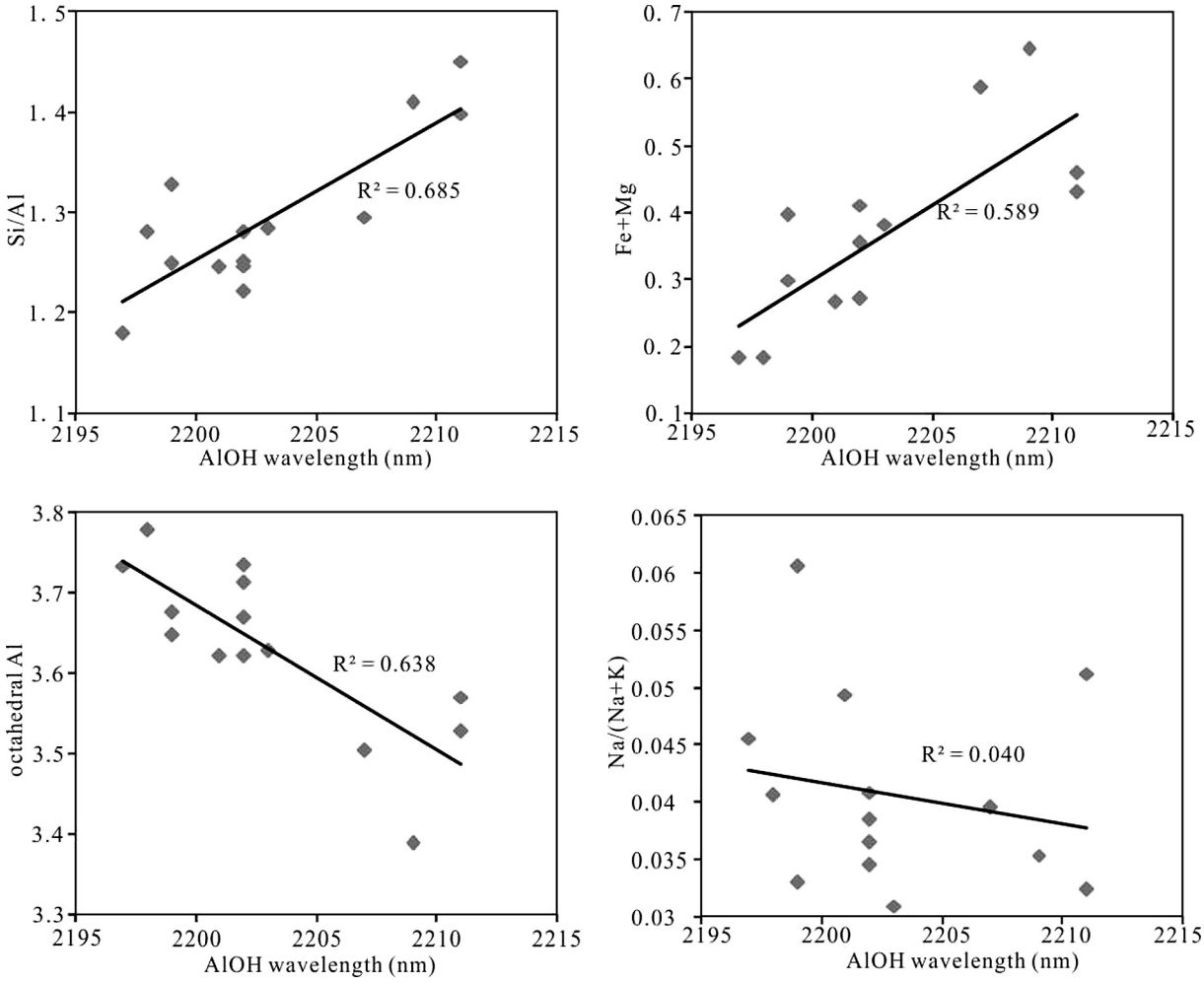

Fig. 9. Binary diagram of the wavelength of the AlOH feature for the Honghai white mica vs. (a) Si/Al; (b) Fe + Mg; (c) octahedral Al; (d) Na/(Na + K).

mula unit (apfu), average Si/Al ratio of 1.26, average Al^{vi} content of 3.68 apfu and average Na/(Na + K) ratio of 0.041. In contrast, samples at the hanging wall Alteration Zones I and II have higher average Fe + Mg content (0.57 apfu), Si/Al ratio (1.43) and lower Al^{vi} content (3.46), Na/(Na + K) ratio (0.030). White mica in one massive sulfide ore sample (sample HH2206-4) shows high Al^{vi} content (3.84 apfu), Na/(Na + K) ratio (0.086), low Fe + Mg content (0.15 apfu) and very low Si/Al ratio (1.16). No useful SWIR data were yielded from the massive sulfide ore samples due to the large amount of sulfides.

6.2.2. Chlorite

The wavelength of the chlorite FeOH absorption feature is present in 372 samples (72.9% of the total samples). The frequency distribution and spectral shift of the FeOH absorption feature wavelengths were illustrated in Fig. 10. Spectral wavelengths of the FeOH absorption feature of the Honghai chlorite range 2249–2261 nm (mean = 2254 nm, median = 2254 nm, n = 639), with most values lie between 2252 and 2257 nm, suggesting that the chlorite compositions vary from being Mg-rich (<2255 nm) to Fe-rich (>2260 nm) (Yang and Huntington, 1996; Jones et al., 2005; Laakso et al., 2016). The average wavelength decrease progressively towards the ore horizon, from Alteration Zones I (2255 nm) and II (2254 nm) to Zone III (2252 nm) (Table 2).

The wavelength variations of the FeOH absorption feature and their zonation in NW cross section were shown in Fig. 11. Relative short wavelengths of the FeOH absorption feature are present close to the ore horizon; however, the trend is not apparent and short wavelengths are also present both in hanging wall and below the massive sulfide lens.

The chlorite spectral results are consistent with the EMPA mineral chemical results (Table 4). An inverse correlation exists between the average FeOH wavelength position and the chlorite Mg/(Fe + Mg) ratio of the same sample (R^2 = 0.587), which indicated that increasing Mg content corresponds to decreasing wavelength of the FeOH absorption feature. Chlorite in the ore proximal zone (Alteration Zone V) with slightly shorter wavelength has an average Mg/(Fe + Mg) ratio of 0.63, whereas that in the ore distal Alteration Zones I and II with longer wavelength has an average Mg/(Fe + Mg) ratios of 0.41 and 0.53, respectively.

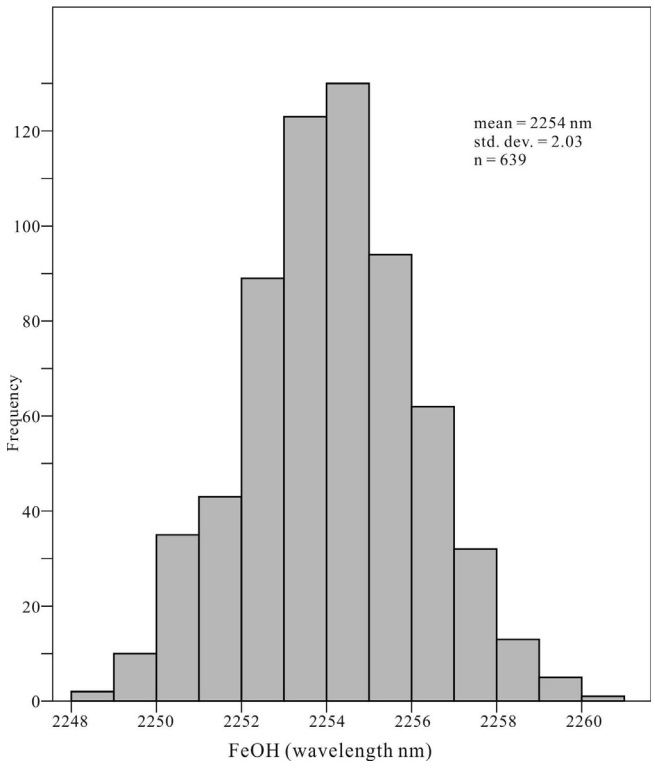

Fig. 10. Histogram of the wavelength range of the FeOH absorption feature for the Honghai chlorite.

7. Discussion

7.1. Metallogeny of the Honghai VMS deposit

7.1.1. Sub-seafloor replacement

It is widely accepted that VMS deposits are resulted from syngenetic hydrothermal systems generated by subvolcanic intrusions (Franklin et al., 2005). Subvolcanic intrusions provide heat to drive hydrothermal convection, and hydrothermal fluids to leach metals from the volcanic and sedimentary rocks. Metal-rich hydrothermal fluids ascend along synvolcanic faults or fissures, mix with the ambient seawater, and precipitate sulfides to form the massive sulfide deposits at or near the seafloor and the stringer zone mineralization underneath (Franklin et al., 2005 and references therein). Many workers also noticed that sub-seafloor replacement may be even more efficient in forming larger and higher grade sulfide deposits (Doyle and Huston, 1999; Doyle and Allen, 2003; Franklin et al., 2005; Piercey, 2015).

Criteria for distinguishing sub-seafloor replacement in VMS deposits include the presence of: (1) host rock remnants in the sulfide deposit; (2) host rock characteristics indicating rapid emplacement; (3) replacement fronts between the sulfide deposit and host rocks; (4) discordance with the enclosing host lithofacies; and (5) strong hanging wall alteration, similar in style and intensity to footwall alteration. Criteria 1 to 3 are diagnostic of replacement-type mineralization, whereas Criteria 4 and 5 may indicate replacement but are not alone diagnostic (Doyle and Allen, 2003).

As for the Honghai deposit, we have found that (1) the boundary between the massive sulfide orebody and host rocks is unstraight, with many sulfide breccias in different size (several centimeters to several meters) being found in the immediate host rocks (Mao et al., 2015, 2016); (2) host rocks include tuffaceous lava, volcanic breccia and breccia-bearing tuff, indicating rapid host rock emplacement; (3) strong phyllic alteration is present in both the footwall and immediate hanging wall; (4) ore textures are dominated by replacement type (Figs. 4 and 6b-c), whereas typical sedimentary pyrite textures (e.g., framboidal and colloform) are scarce; (5) gangue barite veins and patches are present in the massive sulfides (Fig. 6e-f), different from the bedded barite typical to exhalative VMS deposits (Piercey, 2015). These evidences are different from typical exhalative VMS deposits, suggesting an influence of sub-seafloor replacement in the Honghai VMS metallogeny and upgrade the massive sulfides.

7.1.2. Porphyry copper mineralization overprinting

Coeval VMS and porphyry Cu deposits rarely occur together, because of the contrasting extensional and compressional formation tectonics for the former and latter, respectively (Sillitoe, 1980; Franklin et al., 2005). Nevertheless, these two deposit types can coexist in the same arc-backarc systems by terrane juxtaposition (Franklin et al., 2005). Deng et al. (2016) reported both VMS (e.g., Honghai; ca. 440–430 Ma) and porphyry Cu and skarn Fe (e.g., Yudai and Hongshan; ca. 390–380 Ma, Mao, 2014) mineralization in the Kalatag district. Moreover, previous works have compared the geological setting, alteration and mineralization with typical porphyry and epithermal deposits, and proposed that the Kalatag district has the prospecting potential of large porphyry

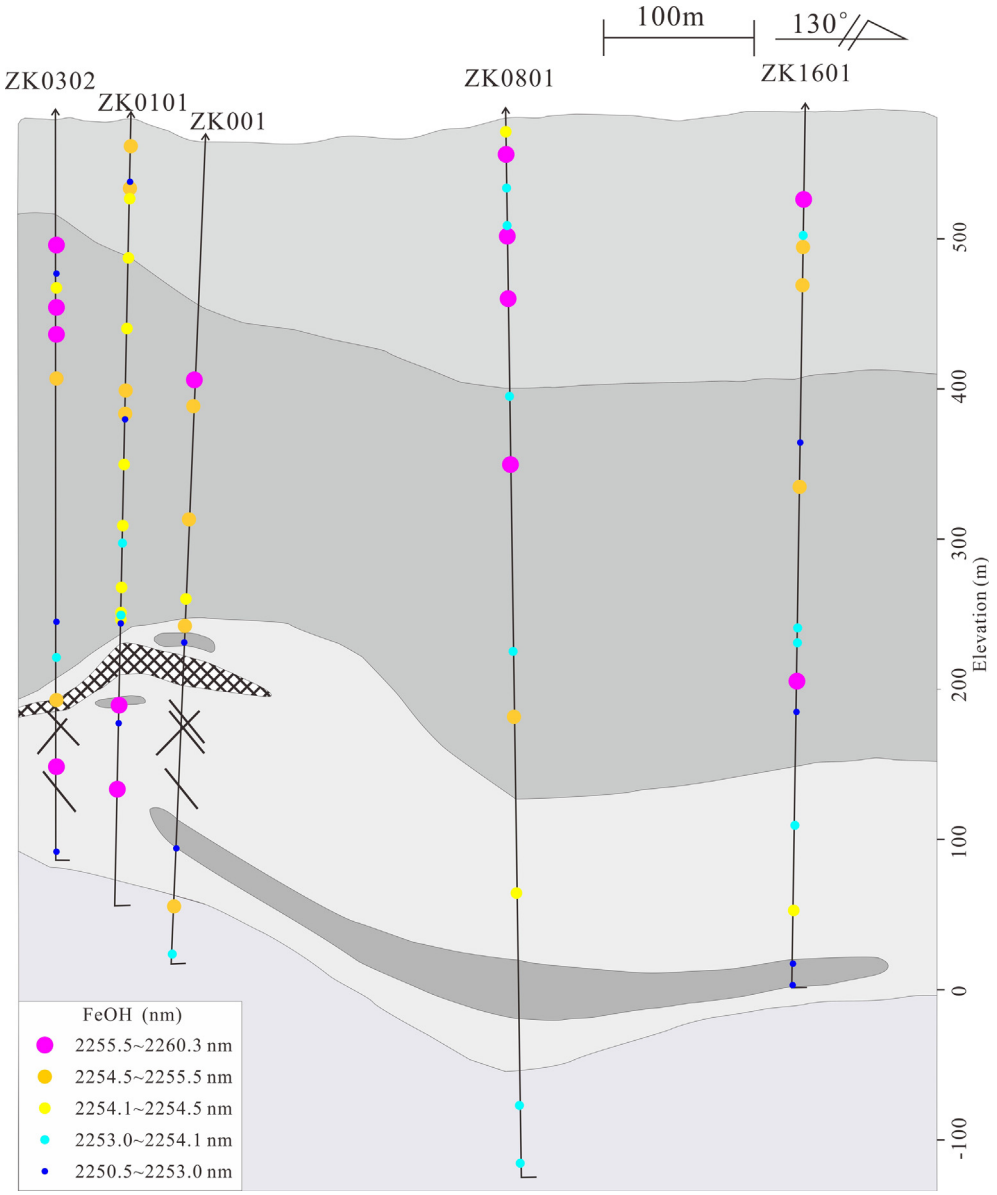

Fig. 11. Wavelength of the FeOH absorption feature of chlorite from the NW section of the Honghai deposit.

and epithermal deposits (Qin et al., 2001; Gao et al., 2006; Miao et al., 2007).

The strong chlorite and epidote alteration in the Honghai hanging wall, and the vein mineral contents (e.g., epidote + quartz + chalcopyrite + bornite, pyrite + hematite + magnetite) (Fig. 12), resemble porphyry-style propylitic alteration (Cooke, 2005; Sillitoe, 2010) and suggest possible late hydrothermal overprint. Strong propylitic alteration only occurred in the hanging wall around the Honghai deposit, whereas footwall was dominated by phyllic and chlorite alteration (both formed in VMS period), and no evident propylitic alteration was found in the footwall and massive sulfide lens. Massive sulfide lens, stockwork mineralization and phyllic alteration are dominated by sulfides, quartz and white mica, lacking of mafic minerals or feldspar, which cannot be likely overprinted by propylitic alteration.

Petrography and EMPA show mark differences between Chlorite I in the proximal Alteration Zones III, V and Chlorite II in the distal Alteration Zones I and II, e.g., the mineral assemblages and features are remarkably different between Chlorite I and II (Figs. 4, 6d, g and l, 12), and Chlorite I is more Mg-rich (higher Mg/(Fe + Mg) ratio) than the Fe-rich Chlorite II (Table 4). Such differences may indicate different hydrothermal events. Therefore, we consider that the hanging wall alteration and mineralization may suggest the margin of ca. 390–380 Ma porphyry Cu mineralization near the Honghai VMS deposit.

7.2. Implications for exploration vectoring

At Honghai, there is a trend of decreasing wavelength of the AlOH absorption feature close to the ore proximal zones (Alteration Zone III), highlighting a shift towards more paragonitic compositions, as also supported by EMPA data (Fig. 8; Table 3).

A similar compositional trend was also documented in the Rosebery, Western Tharsis (Tasmania) and Highway-Reward (Queensland) VMS deposits in Australia (Herrmann et al., 2001), as well as in the Myra Falls (British Columbia) and Izok Lake (Nunavut) VMS deposits in Canada (Jones et al., 2005; van Ruitenbeek et al., 2012; Laakso et al., 2016) (Table 5), whereas the opposite trend is present in other VMS and porphyry copper deposits. At Myra Falls, the wavelengths of the AlOH absorption feature of

Table 4
EMPA results for the Honghai chlorite.

Alteration zone	I			II										V								VI		
Sample no.	ZK0801-6 (5)	ZK1601-2(6)	ZK1601-4(3)	ZK001-3(5)	ZK001-5(5)	ZK001-8(8)	ZK0302-1(5)	ZK0302-6(6)	ZK0302-11(6)	ZK0801-14(4)	ZK0801-19(6)	ZK1601-10(5)	ZK1601-12(10)	ZK001-10(6)	ZK001-20(6)	ZK001-23(6)	ZK001-25(7)	ZK0801-26(5)	ZK0801-28(6)	ZK0302-14(7)	ZK1601-19(5)	ZK0801-32(4)	ZK0302-17(2)	ZK1601-25(11)
FeOH (nm)		2258	2255	2255	2255	2255	2256	2255	2254		2255		2254	2255	2253	2255	2254				2253	2254		2253
wt.%																								
SiO_2	25.11	24.53	26.66	25.92	26.74	25.63	26.09	25.71	25.41	25.73	25.39	26.83	27.78	27.28	27.10	26.19	25.44	26.72	25.75	28.07	27.65	26.72	26.51	26.21
TiO_2	0.00	0.01	0.00	0.00	0.01	0.01	0.01	0.01	0.00	0.00	0.02	0.00	0.01	0.01	0.02	0.02	0.03	0.02	0.02	0.04	0.01	0.03	0.00	0.04
Al_2O_3	20.07	19.32	20.51	19.53	18.72	20.42	19.02	19.27	20.50	19.86	20.90	18.94	18.30	21.01	20.68	21.61	20.32	20.50	20.91	19.64	20.81	20.84	21.34	20.12
FeO	33.66	30.03	25.41	25.93	25.07	25.21	26.89	26.48	25.98	27.33	26.25	21.52	21.23	18.36	18.65	23.40	21.25	19.55	23.37	17.43	17.56	19.81	20.44	24.14
MnO	0.70	1.32	0.45	0.67	0.33	0.36	0.60	0.56	0.45	0.35	0.41	0.39	0.55	0.33	0.69	0.60	0.66	0.57	0.77	0.22	1.52	0.70	0.51	1.03
MgO	9.32	10.36	14.74	14.59	17.05	16.20	14.14	15.13	15.41	15.45	15.31	18.77	19.46	20.08	19.89	16.02	17.85	19.63	16.46	21.60	19.30	18.57	17.78	15.94
CaO	0.05	0.10	0.07	0.05	0.02	0.04	0.08	0.07	0.04	0.04	0.02	0.08	0.05	0.03	0.03	0.01	0.04	0.01	0.03	0.05	0.05	0.02	0.04	0.03
Na_2O	0.02	0.03	0.00	0.01	0.01	0.01	0.03	0.02	0.02	0.02	0.01	0.04	0.01	0.03	0.01	0.01	0.02	0.03	0.02	0.02	0.01	0.01	0.01	0.02
K_2O	0.03	0.07	0.15	0.15	0.09	0.03	0.03	0.02	0.06	0.03	0.01	0.04	0.01	0.04	0.03	0.08	0.02	0.02	0.02	0.09	0.02	0.05	0.20	0.02
Total	89.17	88.16	88.42	87.89	88.22	88.17	88.03	87.90	88.24	88.99	88.54	87.84	87.98	87.49	87.38	88.19	86.91	87.26	87.76	87.55	87.19	87.03	87.27	88.04
apfu (calculated based on the basis of 28 oxygens)																								
Si	5.46	5.34	5.56	5.48	5.58	5.36	5.55	5.46	5.35	5.39	5.32	5.55	5.71	5.53	5.53	5.42	5.33	5.48	5.38	5.67	5.62	5.51	5.46	5.49
Al^{iv}	2.54	2.66	2.44	2.52	2.42	2.64	2.45	2.54	2.65	2.61	2.68	2.45	2.29	2.47	2.47	2.58	2.67	2.52	2.62	2.33	2.38	2.49	2.54	2.51
Al^{vi}	2.60	2.32	2.62	2.37	2.21	2.42	2.33	2.29	2.45	2.32	2.50	2.17	2.16	2.56	2.51	2.71	2.36	2.45	2.54	2.35	2.62	2.58	2.66	2.46
Ti	0.00	0.00	0.00	0.00	0.00	0.00	0.00	0.00	0.00	0.00	0.00	0.00	0.00	0.00	0.00	0.00	0.00	0.00	0.00	0.01	0.00	0.00	0.00	0.01
Fe^{3+}	0.05	0.09	0.12	0.05	0.00	0.00	0.04	0.00	0.00	0.00	0.00	0.00	0.00	0.10	0.06	0.09	0.00	0.02	0.01	0.04	0.17	0.07	0.09	0.03
Fe^{2+}	6.07	5.38	4.31	4.54	4.44	4.46	4.75	4.75	4.64	4.90	4.64	3.74	3.65	3.01	3.12	3.97	3.75	3.34	4.08	2.90	2.82	3.34	3.43	4.20
Mn	0.13	0.24	0.08	0.12	0.06	0.06	0.11	0.10	0.08	0.06	0.07	0.07	0.10	0.06	0.12	0.11	0.12	0.10	0.14	0.04	0.26	0.12	0.09	0.18
Mg	3.02	3.36	4.58	4.60	5.31	5.06	4.49	4.79	4.83	4.83	4.78	5.79	5.97	6.06	6.05	4.95	5.57	6.00	5.13	6.50	5.85	5.71	5.46	4.98
Ca	0.01	0.02	0.02	0.01	0.01	0.01	0.02	0.02	0.01	0.01	0.00	0.02	0.01	0.01	0.01	0.00	0.01	0.00	0.01	0.01	0.01	0.01	0.01	0.01
Na	0.01	0.03	0.00	0.01	0.01	0.01	0.02	0.01	0.01	0.02	0.01	0.03	0.01	0.02	0.01	0.01	0.01	0.02	0.01	0.01	0.01	0.01	0.01	0.01
K	0.02	0.04	0.08	0.08	0.05	0.02	0.02	0.01	0.03	0.01	0.01	0.02	0.01	0.02	0.01	0.04	0.01	0.01	0.01	0.05	0.01	0.02	0.11	0.01
Al total	5.15	4.98	5.06	4.89	4.62	5.05	4.78	4.83	5.10	4.93	5.18	4.63	4.44	5.03	4.98	5.29	5.03	4.97	5.16	4.68	5.00	5.07	5.20	4.97
Fe total	6.12	5.47	4.43	4.59	4.44	4.46	4.79	4.75	4.64	4.90	4.64	3.74	3.65	3.11	3.18	4.05	3.75	3.35	4.09	2.94	2.99	3.42	3.52	4.23
Mg/(Fe + Mg)	0.33	0.38	0.51	0.50	0.54	0.53	0.48	0.50	0.51	0.50	0.51	0.61	0.62	0.66	0.66	0.55	0.60	0.64	0.56	0.69	0.66	0.63	0.61	0.54
Fe/(Fe + Mg)	0.67	0.62	0.49	0.50	0.46	0.47	0.52	0.50	0.49	0.50	0.49	0.39	0.38	0.34	0.34	0.45	0.40	0.36	0.44	0.31	0.34	0.37	0.39	0.46

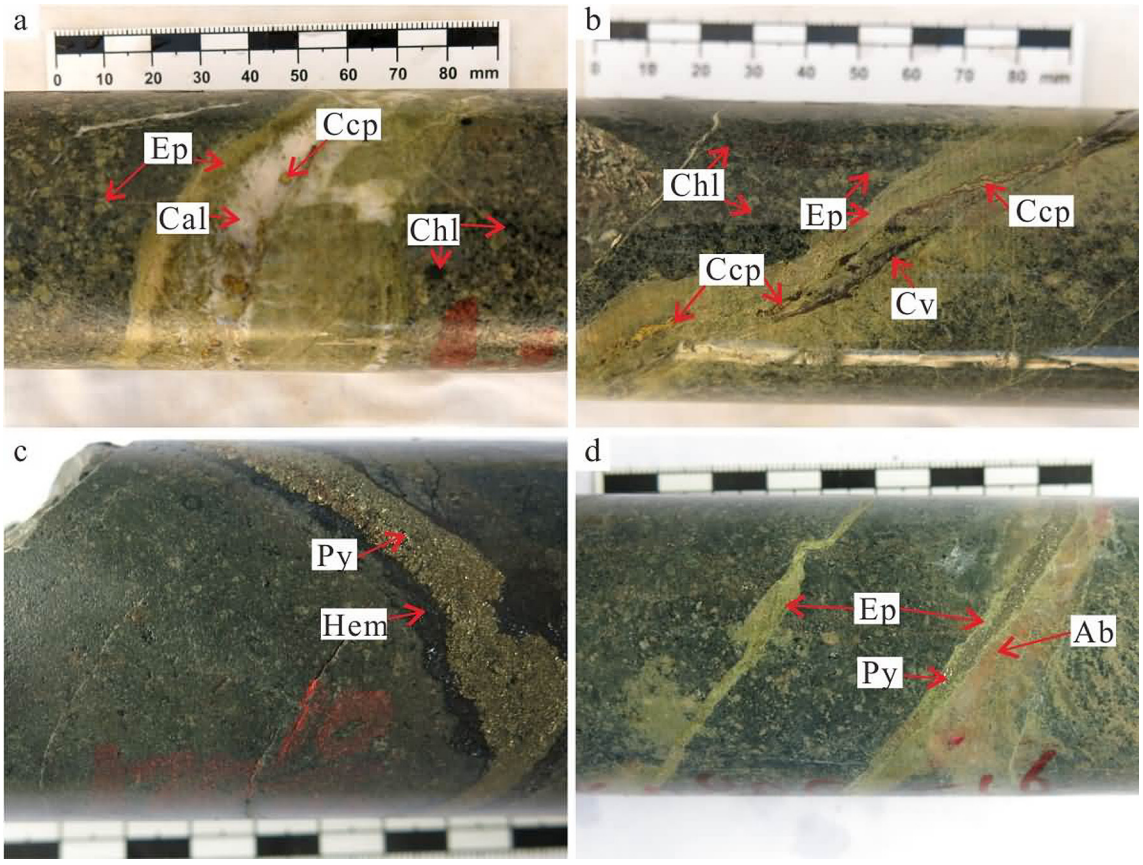

Fig. 12. Photographs showing the propylitic alteration and sulfide veins in the hanging wall of the Honghai deposit. (a) Epidote + calcite + chalcopyrite vein and propylitic alteration; (b) Epidote + chalcopyrite + covellite vein and propylitic alteration; (c) Pyrite + hematite vein; (d) Epidote vein and epidote + pyrite vein.

Table 5
Summary of the spectral and compositions variations for some important VMS and porphyry deposits in the world.

Deposit	Parameter	Proximal zone	Distal zone	Reference
Rosebery (VMS)	AlOH wavelength (nm) Total 2192–2219	2,190–2200	>2200	Herrmann et al. (2001)
	White mica Na/(Na + K) ratio	0.1–0.3	<0.1	
Myra Falls (VMS)	AlOH wavelength (nm)	2194–2204 (avg 2198)	2194–2218 (avg 2206)	Jones et al. (2005)
	White mica Na/(Na + K) ratio	0.05–0.12	0.02–0.06	
	White mica Fe + Mg content	0.13–0.39	0.46–0.77	
	FeOH wavelength (nm)	2238–2252 (avg 2241)	2,238–2255 (avg 2247)	
	Mg/(Mg + Fe) ratio	Avg 0.82	Avg 0.55	
Izok Lake (VMS)	AlOH wavelength (nm): Total 2194–2216	Short; intermediate zone: long	Short	Laakso et al. (2016)
	FeOH wavelength (nm) Total 2244 to 2260	Short, intermediate zone: long	Short	
Hellyer (VMS)	AlOH wavelength (nm)	2202–2222; intermediate zone >2215	Shorter	Yang et al. (2011)
Arroyo Rojo (VMS)	AlOH wavelength (nm) Total 2189–2228	2205–2225	2190–2200	Biel et al. (2012)
	White mica Fe + Mg content	0.42; 0.52 for ore lenses	0.31 for outer zone	
	White mica Si/Al ratio	1.49, 1.54 for ore lenses	1.43 for outer zone	
	White mica Na/(Na + K) ratio	<0.05	0.13	
	FeOH wavelength (nm) Total 2231–2260	<2250	>2260	
	Fe/(Mg + Fe) ratio	0.04–0.26	0.26–0.36	
Tuwu (Porphyry copper deposit)	AlOH wavelength (nm)	2190–2206	2196–2218	Yang et al. (2005)
	FeOH wavelength (nm) Total 2245–2265	Long	Short	
	Fe/(Mg + Fe) ratio	Total 0.7–0.4		
Pebble (Porphyry Cu-Au-Mo deposit)	AlOH wavelength (nm)	Sericite Zone: 2190–2201; intermediate Illite + sericite Zone: 2201–2210	Potassic Zone: 2210–2220	Harraden et al. (2013)

white mica in ore proximal samples range from 2194 to 2204 nm (average = 2198 nm, paragonite-muscovite), whereas the ore distal samples range from 2194 to 2218 nm (average = 2206 nm, muscovite-phengite) (Jones et al., 2005). EMPA indicates that the white mica with shorter wavelengths in the ore proximal samples correspond to slightly sodic compositions (Fe + Mg = 0.13–0.39 apfu; Na/(Na + K) = 0.05–0.12), whereas that with longer wavelengths in the ore distal samples correspond to more phengitic compositions (Fe + Mg = 0.46–0.77 apfu; Na/(Na + K) = 0.02–0.06) (Jones et al., 2005).

The wavelengths of AlOH absorption feature correlate mainly with the proportions of Al^{vi} in the white mica crystal structure (Duke, 1994), with higher Al^{vi} proportions result in shorter wavelengths (Herrmann et al., 2001; Jones et al., 2005). Several kinds of compositional substitutions would affect white mica compositions, including substitutions of Tschermak, Fe-Mg, Na-K and Si^{iv} for $Al^{iv}K$ (Jones et al., 2005). Al^{vi} variation is substantially influenced by Tschermak substitution (Duke, 1994; Jones et al., 2005; van Ruitenbeek et al., 2012), which is in turn controlled by temperature (higher temperature favors Al^{vi} increase and Mg and Fe decrease in white mica) (Miyashiro and Shido, 1985; Duke, 1994; Huston and Kamprad, 2001). High temperature was implied in the vicinity of massive sulfides, which may indicate proximity to hydrothermal fluid conduits, e.g., stringer veins beneath the massive sulfide lens (Gemmell and Large, 1992). In short, for the Honghai white mica, shorter wavelengths of the AlOH absorption feature can vector towards higher temperature zones proximal to the VMS orebody.

Wavelength variation of the FeOH absorption feature is limited for the Honghai chlorite, with slightly longer wavelengths being found in the ore distal Alteration Zones I and II. However, the limited and often ambiguous wavelength variation trends mean that wavelength of the FeOH absorption feature of chlorite is not an effective vector towards the Honghai VMS mineralization center (Fig. 11).

However, chlorites from the Honghai ore proximal and distal zones do show distinct mineralogical and chemical differences. Mg-rich chlorite has also been documented in the ore proximal zones of many important VMS deposits worldwide (Urabe et al., 1983; Large et al., 2001; Jones et al., 2005). Urabe et al. (1983) found that the chlorite Fe/(Fe + Mg) ratio, which increases with distance from the core of alteration pipes, is useful to quantify VMS-style hydrothermal alteration (Gemmell and Large, 1992). According to Hannington et al. (2003), the Mg-rich nature of the chlorite in the ore proximal zone may have been attributed to the influx of seawater.

8. Conclusions

(1) Pervasive and intensive alteration is developed in both the footwall and hanging wall of the Honghai massive sulfide lens. Chlorite and white mica are the dominant alteration minerals, and epidote is typically present in the hanging wall. The alteration/mineralization occurrences (from top to bottom) comprise the chlorite-albite-white mica-carbonate, epidote-chlorite-albite-white mica-carbonate, quartz-white mica-pyrite, massive sulfide, chlorite-pyrite ± white mica and chlorite-quartz-white mica zones

(2) Field geologic and petrographic studies suggested an influence of sub-seafloor replacement in the Honghai VMS metallogeny. Alteration features and ore mineral assemblages in the hanging wall suggested possible porphyry Cu mineralization overprint on the Honghai VMS deposit.

(3) Our new SWIR data confirmed the alteration zonation identified by field geologic and petrographic investigation. The diagnostic wavelengths of the AlOH absorption feature for white mica (2194–2221 nm) are indicative of diverse compositions from slightly paragonite to muscovite and phengite, while the wavelengths of the FeOH absorption feature for chlorite (2249–2261 nm) correspond with Mg-rich to Fe-rich members. Ore proximal zones at Honghai are featured by a decrease in wavelengths of the AlOH absorption feature for white mica, which correspond to high Al^{vi}, low Fe + Mg and Si/Al. No undisputable wavelength trend was identified in the FeOH absorption feature for chlorite, yet the two different generations (Chlorite I and II) distinguished by petrographic observation and EMPA have demonstrated that Mg-rich chlorite is more common in the ore proximal zones.

(4) High Al^{vi} content of white mica in the Honghai ore proximal zone corresponds to higher formation temperature, which may indicate proximity to conduits of the ascending hydrothermal fluids.

(5) SWIR spectral analysis offers an effective and rapid way in identifying alteration minerals. Integrated with field geologic, petrographic and EMPA studies, the SWIR mineral compositional variations can be useful to vector towards VMS mineralization centers in an ore deposit-scale.

Acknowledgements

This study was funded by the Chinese National Basic Research 973 Program (2014CB440802), CAS-SAFEA International Partnership Program for Creative Research Teams (20140491534), CAS Creative and Interdisciplinary Program (Y433131A07), CAS 100 Talent Program (Y333081A07), National Natural Science Foundation of China (41572077), SKL-ODG open funds (201508) and China Geological Survey Bureau (121201004000150017-43). We would like to thank Dr. Zhiming Yang (CAGS) for providing the TerraSpec equipment for the SWIR spectral analyses. The Hongshi copper mining staff were thanked for their help in field investigation. We thank Dr. Weifeng Zhang, Chao Xu and Bing Xiao (GIGCAS) for kindly discussion and suggestions. Comments and suggestions from editor and reviewers greatly improved the quality of the paper.

References

Biel, C., Subías, I., Acevedo, R.D., Yusta, I., Velasco, F., 2012. Mineralogical, IR-spectral and geochemical monitoring of hydrothermal alteration in a deformed and metamorphosed Jurassic VMS deposit at Arroyo Rojo, Tierra del Fuego, Argentina. J. S. Am. Earth Sci. 35, 62–73.

Chang, Z.S., Hedenquist, J.W., White, N.C., Cooke, D.R., Roach, M., Deyell, C.L., Garcia, J., Gemmell, J.B., McKnight, S., Cuison, A.L., 2011. Exploration tools for linked porphyry and epithermal deposits: example from the Mankayan intrusion-centered Cu-Au District, Luzon, Philippines. Econ. Geol. 106, 1365–1398.

Chang, Z.S., Yang, Z.M., 2012. Evaluation of inter-instrument variations among short wavelength infrared (SWIR) devices. Econ. Geol. 107, 1479–1488.

Chen, Y.J., Pirajno, F., Wu, G., Qi, J.P., Xiong, X.L., 2012. Epithermal deposits in North Xinjiang, NW China. Int. J. Earth Sci. 101, 889–917.

Cooke, D.R., 2005. Giant porphyry deposits: characteristics, distribution, and tectonic controls. Econ. Geol. 100, 801–818.

Deng, X.H., Wang, J.B., Wang, Y.W., Li, Y.C., Fang, T.H., Mao, Q.G., 2014. Geological characteristics of the Hongshi Cu-Au deposit, Eastern Tianshan, Xinjiang and discussion of the deposit genesis. Miner. Explor. 5, 159–168 (in Chinese with English abstract).

Deng, X.H., Wang, J.B., Pirajno, F., Wang, Y.W., Li, Y.C., Li, C., Zhou, L.M., Chen, Y.J., 2016. Re–Os dating of chalcopyrite from selected mineral deposits in the Kalatag district in the Eastern Tianshan Orogen, China. Ore Geol. Rev. 77, 72–81.

Deng, X.H., Wang, J.B., Santosh, M., Li, Y.C., Wang, Y.W., Mao, Q.G., Long, L.L., Chen, X., 2018. New 40Ar/39Ar ages from the Kalatag district in the Eastern Tianshan, NW China: constraints on the timing of Cu mineralization and stratigraphy. Ore Geol. Rev. 100, 250–262.

Doyle, M.G., Huston, D.L., 1999. The subsea-floor replacement origin of the Ordovician Highway-Reward volcanic-associated massive sulfide deposit, Mount Windsor Subprovince, Australia. Econ. Geol. 94, 825–843.

Doyle, M.G., Allen, R.L., 2003. Subsea-floor replacement in volcanic-hosted massive sulfide deposits. Ore Geol. Rev. 23, 183–222.
Duke, E.F., 1994. Near infrared spectra of muscovite, Tschermak substitution, and metamorphic reaction progress: implications for remote sensing. Geology 22, 621–624.
Franklin, J.M., Lydon, J., Sangster, D.F., 1981. Volcanic-associated massive sulfide deposits. Econ. Geol. 75, 485–627.
Franklin J.M., Gibson H.L., Jonasson I.R., Galley A.G., 2005. Volcanogenic massive sulfide deposits. Economic Geology 100th Anniversary, vol. 98, 523–560.
Galley, A.G., Hannington, M.D., Jonasson, I.R., 2007. Volcanogenic massive sulphide deposits. Mineral deposits of Canada: A synthesis of major deposit-types, district metallogeny, the evolution of geological provinces, and exploration methods: Geological Association of Canada. Mineral Deposits Division, Special Publication 5, 141–161.
Gao, Z.Q., Fang, W.X., Hu, R.Z., Liu, J.S., 2006. The metallogenic environment of Kalatage porphyry copper (gold) deposit and its prospecting perspective, Xinjiang, China. Acta Geol. Sinica 80, 90–100 (in Chinese with English abstract).
Gemmell, J.B., Large, R.R., 1992. Stringer system and alteration zones underlying the Hellyer volcanogenic massive sulfide deposit, Tasmania, Australia. Econ. Geol. 87, 620–649.
Gemmell, J.B., Herrmann, W., 2001. A special issue on alteration associated with volcanic-hosted massive sulfide deposits, and its exploration significance. Econ. Geol. 96, 909–912.
Hannington, M., Kjarsgaard, I., Galley, A., Taylor, B., 2003. Mineral-chemical studies of metamorphosed hydrothermal alteration in the Kristineberg volcanogenic massive sulfide district, Sweden. Miner. Deposita 38, 423–442.
Harraden, C.L., Mcnulty, B.A., Gregory, M.J., Lang, J.R., 2013. Shortwave infrared spectral analysis of hydrothermal alteration associated with the Pebble porphyry copper-gold-molybdenum deposit, Iliamna, Alaska. Econ. Geol. 108, 483–494.
Herrmann, W., Blake, M., Doyle, M., Huston, D., Kamprad, J., Merry, N., Pontual, S., 2001. Short wavelength infrared (SWIR) spectral analysis of hydrothermal alteration zones associated with base metal sulfide deposits at Rosebery and Western Tharsis, Tasmania, and Highway-Reward, Queensland. Econ. Geol. 96, 939–955.
Hey, M.H., 1954. A new review of the chlorites. Mineral. Mag. 30, 277–292.
Huston, D.L., Kamprad, J., 2001. Zonation of alteration facies at Western Tharsis: implications for the genesis of Cu-Au deposits, Mount Lyell Field, Western Tasmania. Econ. Geol. 96, 1123–1132.
Jahn, B.M., Wu, F.Y., Chen, B., 2000. Massive granitoid generation in Central Asia: Nd isotope evidence and implication for continental growth in the Phanerozoic. Episodes 23, 82–92.
Jones, S., Herrmann, W., Gemmell, J.B., 2005. Short wavelength infrared spectral characteristics of the HW Horizon: implications for exploration in the Myra Falls volcanic-hosted massive sulfide camp, Vancouver Island, British Columbia, Canada. Econ. Geol. 100, 273–294.
Kranidiotis, P., MacLean, W.H., 1987. Systematics of chlorite alteration at the Phelps Dodge massive sulfide deposit, Matagami, Quebec. Econ. Geol. 82, 1898–1911.
Laakso, K., Rivard, B., Peter, J.M., White, H.P., Maloley, M., Harris, J., Rogge, D., 2015. Application of airborne, laboratory, and field hyperspectral methods to mineral exploration in the Canadian Arctic: recognition and characterization of volcanogenic massive sulfide-associated hydrothermal alteration in the Izok Lake deposit area, Nunavut, Canada. Econ. Geol. 110, 925–941.
Laakso, K., Peter, J.M., Rivard, B., White, H.P., 2016. Short-wave infrared spectral and geochemical characteristics of hydrothermal alteration at the Archean Izok Lake Zn-Cu-Pb-Ag volcanogenic massive sulfide deposit, Nunavut, Canada: Application in exploration target vectoring. Econ. Geol. 111, 1223–1239.
Large, R.R., 1992. Australian volcanic-hosted massive sulfide deposits: features, styles, and genetic models. Econ. Geol. 87, 471–510.
Large, R.R., McPhie, J., Gemmell, J.B., Herrmann, W., Davidson, G.J., 2001. The spectrum of ore deposit types, volcanic environments, alteration halos, and related exploration vectors in submarine volcanic successions: Some examples from Australia. Econ. Geol. 96, 913–938.
Li, W.Q., Wang, R., Wang, H., Xia, B., 2006. Geochemistry and petrogenesis of the Kalata intrusion in the "Tuha window". Geol. China 33, 559–565 (in Chinese with English abstract).
Mao, Q.G., Fang, T.H., Wang, J.B., Wang, S.L., Wang, N., 2010. Geochronology studies of the Early Paleozoic Honghai massive sulfide deposits and its geological significance in Kalatage area, Eastern Tianshan Mountain. Acta Petrol. Sinica 26, 3017–3026 (in Chinese with English abstract).
Mao, Q.G., 2014. The geological, metallogenesis and metallogenic prognosis studies of the Kalatage copper polymetallic ore district in eastern Tianshan, NW China. Post-Doctoral Research Report, 1–154 (in Chinese).
Mao, Q.G., Wang, J.B., Fang, T.H., Zhu, J.J., Fu, W.W., Yu, M.J., Huang, X.K., 2015. Lead and sulfur isotope studies of sulfides from Honghai VMS-type deposit in Kalatage ore belt of eastern Tianshan Mountains. Miner. Deposits 34, 730–744 (in Chinese with English abstract).
Mao, Q.G., Wang, J.B., Fang, T.H., Yu, M.J., Zhu, J.J., Zhang, R., Fu, W.W., Gao, W.H., 2016. Geological characteristics of Honghai VMS type deposit of Kalatage ore belt and discussion of genesis type in the eastern Tianshan. Miner. Explor. 7, 17–30 (in Chinese with English abstract).
Miao, Y., Qin, K.Z., Xu, Y.X., Fang, T.F., Ding, K.S., Xu, X.W., 2007. Geological and fluid inclusion characteristics of Meiling Cu-Au deposit in Kalatage ore belt, Eastern Xinjiang, in comparison with typical Zijinshan-style HS-epithermal deposit. Miner. Deposits 26, 79–88 (in Chinese with English abstract).
Miyashiro, A., Shido, F., 1985. Tschermak substitution in low- and middle-grade pelitic schists. J. Petrol. 26, 449–487.
Piercey, S.J., 2015. A semipermeable interface model for the genesis of subseafloor replacement-type volcanogenic massive sulfide (VMS) deposit. Econ. Geol. 110, 1655–1660.
Qin, K.Z., Fang, T.H., Wang, S.L., Wang, X.D., 2001. The discovery and metallogenic potential of Kalatage Cu-Au mineralization district in the Paleozoic "window", southern margin of Tuha Basin. Geol. China 28, 16–23 (in Chinese).
Sengör, A.M.C., Natal'In, B.A., Burtman, V.S., 1993. Evolution of the Altaid tectonic collage and Palaeozoic crustal growth in Eurasia. Nature 364, 299–307.
Shen, P., Pan, H.D., Zhou, T.F., Wang, J.B., 2014. Petrography, geochemistry and geochronology of the host porphyries and associated alteration at the Tuwu Cu deposit, NW China: a case for increased depositional efficiency by reaction with mafic hostrock? Miner. Deposita 49, 709–731.
Sillitoe, R.H., 1980. Are porphyry copper and Kuroko-type massive sulfide deposits incompatible? Geology 8, 11–14.
Sillitoe, R.H., 2010. Porphyry copper systems. Econ. Geol. 105, 3–41.
Tappert, M.C., Rivard, B., Giles, D., Tappert, R., Mauger, A., 2013. The mineral chemistry, near-infrared, and mid-infrared reflectance spectroscopy of phengite from the Olympic Dam IOCG deposit, South Australia. Ore Geol. Rev. 53, 26–38.
Thompson, A.J., Hauff, P.L., Robitaille, A.J., 1999. Alteration mapping in exploration: application of short-wave infrared (SWIR) spectroscopy. SEG Newsl. 39, 16–27.
Urabe, T., Scott, S.D., Hattori, K., 1983. A comparison of footwall-rock alteration and geothermal systems beneath some Japanese and Canadian volcanogenic massive sulfide deposits. Econ Geol Monogr. 5, 345–364.
van Ruitenbeek, F.J.A., Cudahy, T., Hale, M., van der Meer, F.D., 2005. Tracing fluid pathways in fossil hydrothermal systems with near-infrared spectroscopy. Geology 33, 597–600.
van Ruitenbeek, F.J., Cudahy, T.J., van der Meer, F.D., Hale, M., 2012. Characterization of the hydrothermal systems associated with Archean VMS-mineralization at Panorama, Western Australia, using hyperspectral, geochemical and geothermometric data. Ore Geol. Rev. 45, 33–46.
Wang, J.B., Wang, Y.W., He, Z.J., 2006. Ore deposits as a guide to the tectonic evolution in the East Tianshan Mountains, NW China. Geol. China 33, 461–469 (in Chinese with English abstract).
Xiao, W.J., Windley, B.F., Allen, M.B., Han, C.M., 2013. Paleozoic multiple accretionary and collisional tectonics of the Chinese Tianshan orogenic collage. Gondwana Res. 23, 1316–1341.
Yang K., Huntington J.F., 1996. Spectral signatures of hydrothermal alteration in the metasediments at Dead Bullock Soak, Tanami Desert, Northern Territory. CRISO/AMIRA Project P435, 1–29.
Yang, K., Lian, C., Huntington, J.F., Peng, Q., Wang, Q., 2005. Infrared spectral reflectance characterization of the hydrothermal alteration at the Tuwu Cu–Au deposit, Xinjiang, China. Miner. Deposita 40, 324–336.
Yang, K., Huntington, J.F., Gemmell, J.B., Scott, K.M., 2011. Variations in composition and abundance of white mica in the hydrothermal alteration system at Hellyer, Tasmania, as revealed by infrared reflectance spectroscopy. J. Geochem. Explor. 108, 143–156.
Yang, Z.M., Hou, Z.Q., Yang, Z.S., Qu, H.C., Li, Z.Q., Liu, Y.F., 2012. Application of short wavelength infrared (SWIR) technique in exploration of poorly eroded porphyry Cu district: a case study of Niancun ore district, Tibet. Miner. Deposits 31, 699–717 (in Chinese with English abstract).
Zheng, J.H., Mao, J.W., Yang, F.Q., Liu, F., Zhu, Y.F., 2015. The post-collisional Cihai iron skarn deposit, Eastern Tianshan, Xinjiang, China. Ore Geol. Rev. 67, 244–254.